Materials and Design 195 (2020) 108970

Contents lists available at ScienceDirect

Materials and Design

journal homepage: www.elsevier.com/locate/matdes

Deep neural network approach to estimate biaxial stress-strain curves of sheet metals

Akinori Yamanaka [a,*], Ryunosuke Kamijyo [b], Kohta Koenuma [b], Ikumu Watanabe [c], Toshihiko Kuwabara [a]

[a] Division of Advanced Mechanical Systems Engineering, Institute of Engineering, Tokyo University of Agriculture and Technology, 2-24-16, Naka-cho, Koganei-shi, Tokyo 184-8588, Japan
[b] Department of Mechanical Systems Engineering, Graduate School of Engineering, Tokyo University of Agriculture and Technology, 2-24-16, Naka-cho, Koganei-shi, Tokyo 184-8588, Japan
[c] Research Center for Structural Materials, National Institute of Materials Science, 1-2-1 Sengen, Tsukuba, Ibaraki 305-0047, Japan

HIGHLIGHTS

- DNNs were used to estimate biaxial stress-strain curves of aluminum alloy sheets.
- Pole figure images and 3D orientation maps were explored as input data.
- DNNs were as accurate as numerical biaxial tensile tests, but much faster.
- A new approach to virtual data generation for material modeling was demonstrated.

GRAPHICAL ABSTRACT

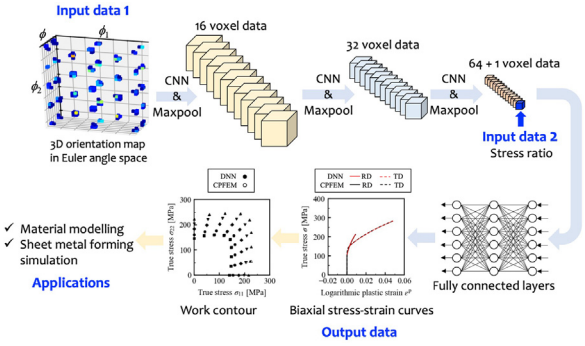

ARTICLE INFO

Article history:
Received 20 May 2020
Received in revised form 1 July 2020
Accepted 9 July 2020
Available online 15 July 2020

Keywords:
Deep neural network
Material modeling
Multiaxial material testing
Aluminum alloy sheets

ABSTRACT

To improve the accuracy of a sheet metal forming simulation, the constitutive model is calibrated using results from multiaxial material testing. However, multiaxial material testing is time-consuming and requires specialized equipment. This study proposes two different deep neural network (DNN) approaches, a two- and three-dimensional convolutional neural network (DNN-2D and DNN-3D), to efficiently estimate biaxial stress-strain curves of aluminum alloy sheets from a digital image representing the sample's crystallographic texture. DNN-2D is designed to estimate biaxial stress-strain curves from a digital image of {111} pole figure, while DNN-3D estimates the curves from a 3D image of the texture. The two DNNs were trained using synthetic texture datasets and the corresponding biaxial stress-strain curves obtained from crystal plasticity-based numerical biaxial tensile tests. The accuracy of the two trained DNNs was examined by comparing the results from that of the numerical biaxial tensile tests. It was observed that both the DNNs could estimate biaxial stress-strain curves with high accuracy. Though DNN-3D provides with a better estimation than DNN-2D, it displays lower computational efficiency. Thus, the two DNNs and their training procedures offer a new and efficient method to provide virtual data for material modeling.

1. Introduction

Commercial finite element simulation software is widely used in industry to simulate sheet metal forming process [1,2]. Many phenomenological constitutive models based on yield functions have been developed and incorporated into commercial finite element software

* Corresponding author.
E-mail address: a-yamana@cc.tuat.ac.jp (A. Yamanaka).

https://doi.org/10.1016/j.matdes.2020.108970

over the past decades [3–8]. The precise prediction of defects (e.g. fracture and springback) using sheet metal forming simulations relies on the accuracy of the yield function, the constitutive model, and its parameters (i.e. material model which should reproduce the actual plastic deformation behavior). The material model can be calibrated using various multiaxial material testing methods [9] that measures the plastic deformation behavior of sheet metals under multiaxial stress conditions like the hydraulic bulge [10], stack compression [11], biaxial tensile test (cruciform sample) [12–14], and multiaxial tube expansion tests [15]. The calibrations are generally performed based on the contour of equal plastic work and the direction of incremental plastic strain rates measured by multiaxial material tests. Therefore, acquisition of experimental data by multiaxial material tests is key to obtain highly accurate sheet metal forming simulation results [16–18].

The crystal plasticity finite element method (CPFEM) is another popular method for simulating the plastic deformation behavior of sheet metals during metal forming process [19,20]. Previous studies of sheet metal forming simulations using CPFEM have investigated deep drawing and spherical punch forming [21–26]. However, CPFEM-based sheet metal forming simulations have not been widely adopted in the industry due to the high computational demand of the method, despite the use of high-performance computers.

Crystal plasticity-based simulations can also be used in virtual material testing [27] and virtual laboratory [28]. In virtual material testing, a material model is calibrated using the results from crystal plasticity-based simulations instead of time-consuming experimental multiaxial material tests. Hence, virtual material testing has been widely applied to calibrate material models of sheet metals [27,29–36]. However, calculating the contour of equal plastic work and the yield locus using virtual material testing requires the use of user-developed source codes for crystal plasticity simulations, thus involving a high computational load.

Machine-learning is an effective way to estimate the mechanical response of materials from their microstructural information. Many machine-learning algorithms have been proposed, where artificial neural networks (ANNs) have gained popularity in the field of materials science since the 1990s [37–39]. An early review article by Bhadeshia [39] published in 1999 had already anticipated that ANN will be a promising machine-learning tool for estimating material properties. In fact, ANNs have since been applied widely for the estimation of mechanical behavior for various materials [40–45]. Yang et al. [43] proposed a new methodology to predict the stress-strain curve of binary composites using ANN and principal component analysis. Janab et al. [44] used a genetic algorithm and ANN to predict the rate-dependent tensile flow behavior of AA5182-O aluminum alloy sheets. More recently, Ali et al. [45] employed ANN to estimate the stress-strain curve and texture evolution of AA6063-T6 aluminum alloy under non-proportional loading conditions.

We have previously proposed a deep neural network (DNN)-based methodology for the estimation of uniaxial stress-strain curves and the anisotropy of Lankford value (*r*-value) of aluminum alloy sheets using crystallographic texture data [46]. In the previous study, DNN was trained with a large training dataset generated using crystal plasticity finite element simulations of uniaxial tensile testing, referred to as numerical material tests [32]. The trained DNN successfully estimated the uniaxial stress-strain curve and anisotropic evolution of *r*-value with the same accuracy as numerical material tests [46]. However, to the best of the author's knowledge, machine-learning-based methodology has not yet been used to estimate biaxial stress-strain curves of sheet metals.

The purpose of this study is to propose a new DNN approach to efficiently estimate biaxial stress-strain curves of sheet metals from their underlying microstructural features. Two DNNs were developed; one to estimate biaxial stress-strain curves from a digital image of {111} pole figure (DNN-2D) and another to estimate biaxial stress-strain curves from a three-dimensional (3D) image representing the crystallographic texture in a voxelized Euler angle space (DNN-3D). Both the DNNs were trained using synthetic crystallographic texture datasets containing typical preferred texture components in aluminum alloy sheets, namely Cube, Goss, S, Brass, and Copper-components. Biaxial stress-strain curves, used in the training dataset, were generated via CPFEM based numerical biaxial tensile tests. The two trained DNNs were validated by comparing the estimated biaxial stress-strain curves with those obtained from numerical biaxial tensile tests. To facilitate further implementation of this proposed DNN approach, the trained DNNs, training parameters, and training datasets are made available for free download at https://github.com/Yamanaka-Lab-TUAT/DNN-NMT [47].

2. Materials and methods

2.1. Experimental tensile testing

The numerical biaxial tensile tests, used to generate the training dataset, were validated using experimental uniaxial and biaxial tensile testing of a 5182-O aluminum alloy sheet (initial thickness = 1.0 mm). The crystallographic texture of the sheet was measured using electron backscattered diffraction (EBSD). The number of crystal orientations obtained from the EBSD measurement was 1,009,957. The {111} pole figure of the measured texture is given in Fig. 1. The pole figure indicated that the texture in the 5182-O aluminum alloy sheet included a weak {001}⟨100⟩ Cube-component.

The true stress-true strain curve obtained from the uniaxial tensile test was used to identify the parameters in the crystal plasticity constitutive equation used in the numerical biaxial tensile tests. The uniaxial tensile samples were prepared in accordance with the Japan Industrial Standards (JIS 13 B-type specimen). The rolling direction (RD) of the sheet was set parallel to the tensile direction in the uniaxial tensile test. The uniaxial tensile tests were performed using the Autograph AG-Xplus 100 kN instrument (SHIMADZU Co.). A fixed equivalent plastic strain rate in the order of $5.0 \times 10^{-4}\ s^{-1}$ was used during uniaxial tensile testing under a quasi-static condition. Two specimens each were tested for RD and transverse direction (TD) of the sheet.

The biaxial tensile tests were performed on cruciform samples using a servo-controlled testing machine. The detailed specifications of the samples and testing machine have been previously reported [14,15]. Tensile forces were applied along RD and TD of the sheet and various ratios of the true stress components along the RD and TD (σ_{11}: σ_{22} = 4:1, 2:1, 4:3, 1:1, 3:4, 1:2, and 1:4, where σ_{11} and σ_{22} correspond to the true stress along RD and TD, respectively) on a linear stress path were investigated. A fixed equivalent strain rate in the order of $5.0 \times 10^{-4}\ s^{-1}$ was used during biaxial tensile testing. Two specimens were tested for each stress ratio and the two stress-strain curves thus obtained from the biaxial tensile tests were averaged. The averaged biaxial stress-strain curves were compared to those calculated from the numerical biaxial tensile tests.

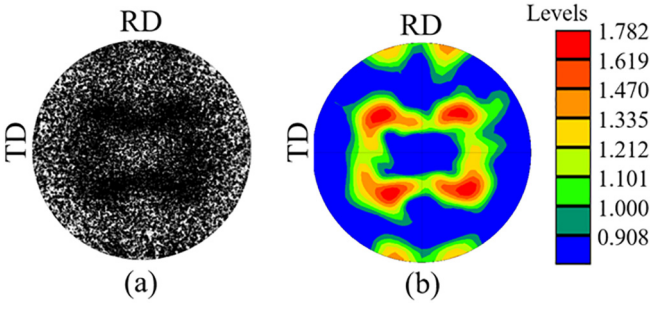

Fig. 1. {111} pole figure of crystallographic texture in a 5182-O aluminum alloy sheet (a) measured using EBSD and (b) illustrated as a density plot.

2.2. Numerical biaxial tensile testing

The constitutive equation based on the crystal plasticity theory [48–51] and the finite element model used in the numerical biaxial tensile tests are presented in this section.

2.2.1. Crystal plasticity constitutive equation

The crystal plasticity constitutive equation proposed by Peirce et al. [48] was used in our study. Multiplicative decomposition of a deformation gradient tensor (F_{ij}) in the Cartesian coordinate system gives the following equation:

$$F_{ij} = F^*_{ik}F^p_{kj} \tag{1}$$

where F^*_{ik} and F^p_{kj} are the elastic and the plastic components of the deformation gradient tensor, respectively. The velocity gradient tensor (L_{ij}) is defined as:

$$L_{ij} = \dot{F}_{ik}F^{-1}_{kj} \tag{2}$$

where $\dot{F}_{ik}$ is the rate of the deformation gradient tensor. The velocity gradient tensor in Eq. (2) can be divided into two tensors as:

$$L_{ij} = D_{ij} + W_{ij} \tag{3}$$

where D_{ij} is the deformation rate tensor and W_{ij} is the continuum spin tensor. These tensors are comprised of elastic and plastic components:

$$D_{ij} = D^e_{ij} + D^p_{ij} \tag{4}$$

$$W_{ij} = W^*_{ij} + W^p_{ij} \tag{5}$$

where D^e_{ij} and D^p_{ij} are the elastic and plastic components of the deformation rate tensor, respectively and W^*_{ij} and W^p_{ij} are the elastic and plastic components of the spin tensor, respectively. The plastic components of the deformation rate and the spin tensors are described as:

$$D^p_{ij} = \sum_{\alpha=1}^{n_{slip}} P^{(\alpha)}_{ij}\dot{\gamma}^{(\alpha)} \tag{6}$$

$$W^p_{ij} = \sum_{\alpha=1}^{n_{slip}} \omega^{(\alpha)}_{ij}\dot{\gamma}^{(\alpha)} \tag{7}$$

where n_{slip} is the number of slip systems in a crystal and $\dot{\gamma}\ (\alpha)$ is the plastic shear strain rate for the αth slip system. As 12 slip systems are involved in a face-centered cubic crystal, we have $n_{slip} = 12$ and α can vary from 1 to 12. We have used the following equation proposed by Pan et al. [49] to calculate the plastic shear strain rate:

$$\dot{\gamma}^{(a)} = \dot{\gamma}_0 \frac{\tau^{(a)}}{g^{(a)}}\left|\frac{\tau^{(a)}}{g^{(a)}}\right|^{\frac{1}{m}-1} \tag{8}$$

where $\dot{\gamma}_0$ is the reference shear strain rate, $\tau^{(\alpha)}$ is the resolved shear stress for αth slip system, m is the strain rate sensitivity parameter, and $g^{(\alpha)}$ is the critical resolved shear stress (CRSS) for αth slip system. Further, $P^{(\alpha)}_{ij}$ and $\omega^{(\alpha)}_{ij}$ in Eqs. (6) and (7) are given as follows:

$$P^{(\alpha)}_{ij} = \frac{1}{2}\left(s^{*(\alpha)}_i m^{*(\alpha)}_j + m^{*(\alpha)}_i s^{*(\alpha)}_j\right) \tag{9}$$

$$\omega^{(\alpha)}_{ij} = \frac{1}{2}\left(s^{*(\alpha)}_i m^{*(\alpha)}_j - m^{*(\alpha)}_i s^{*(\alpha)}_j\right) \tag{10}$$

where $s^{*(\alpha)}_i\ (i = 1, 2, 3)$ is a unit vector in the slip direction and $m^{*(\alpha)}_i$ is a unit vector normal to the slip plane in the deformed configuration. The crystal rotation was described as follows:

$$s^{*(\alpha)}_i = F^*_{ij}s^{0(\alpha)}_j \tag{11}$$

$$m^{*(\alpha)}_i = m^{0(\alpha)}_j F^{*-1}_{ji} \tag{12}$$

where $m^{0(\alpha)}_i$ is a unit vector in the direction of initial slip and $s^{0(\alpha)}_i$ is a unit vector normal to the slip plane.

The constitutive equation for finite deformation is given as:

$$\overset{\nabla}{\sigma}_{ij} = C^e_{ijkl}D_{kl} - \sum_{\alpha=1}^{n_{slip}} R^{(\alpha)}_{ij}\dot{\gamma}^{(\alpha)} \tag{13}$$

Further,

$$R^{(\alpha)}_{ij} = \omega^{(\alpha)}_{ik}\sigma_{kj} - \sigma_{ik}\omega^{(\alpha)}_{kj} + C^e_{ijkl}P^{(\alpha)}_{kl} \tag{14}$$

where $\nabla\sigma_{ij}$ is the Jaumann rate of the Cauchy stress tensor and C^e_{ijkl} is the elastic modulus tensor.

The evolution of CRSS was used to evaluate the strain-hardening of the material by employing the following equation:

$$g^{(a)} = \tau_0 + \int_t \dot{g}^{(a)}dt \tag{15}$$

where t denotes time and τ_0 is the initial CRSS. $\dot{g}\ (\alpha)$ is the rate of CRSS, and is defined as:

$$\dot{g}^{(\alpha)} = \sum_{\beta=1}^{n_{slip}} h^{(\alpha\beta)}\left|\dot{\gamma}^{(\beta)}\right| \tag{16}$$

where $h^{(\alpha\beta)}$ is the hardening coefficient matrix. This term is further defined as:

$$h^{(\alpha\beta)} = q^{(\alpha\beta)}\frac{d\tau(\gamma)}{d\gamma} + \left(1 - q^{(\alpha\beta)}\right)\frac{d\tau(\gamma)}{d\gamma}\delta_{\alpha\beta} \tag{17}$$

where $q^{(\alpha\beta)}$ is a matrix describing the level of latent-hardening and $\delta_{\alpha\beta}$ is the Dirac delta function. The relationship between the shear stress and the accumulated plastic shear strain (γ) is given as:

$$\tau(\gamma) = \tau_0 + h_0\{C(\gamma_{\text{int}} + \gamma)\}^{n'} \tag{18}$$

where h_0 is the initial hardening coefficient, n' is the hardening index, C is the hardening constant, and γ_{int} is the initial plastic shear strain. The parameters used to describe the strain-hardening behavior of the test sample included τ_0, h_0, n', C, and γ_{int}. These parameters were calibrated by fitting the uniaxial stress-strain curve for RD (i.e. σ_{11}: $\sigma_{22} = 1{:}0$) calculated from the numerical biaxial tensile test to the reference experimental uniaxial tensile test data.

The mathematical homogenization method [52,53] was used to calculate the biaxial stress-strain curves of aluminum alloy sheets based on the underlying crystallographic texture of the samples using numerical biaxial tensile tests. The homogenization method derives the governing equations for two-scale boundary value problems (BVPs) in both microscopic and macroscopic length-scales. The microscale BVP was solved using finite element method and the microscale mechanical behavior of the microstructure was analyzed in specific macroscopic stress states. Further, the macroscopic mechanical behavior was evaluated at each integration point of the macroscale finite element model using the microscale BVP solutions. This micro-macro coupling scheme has been widely applied in the finite element modeling of elastoplastic materials [53–56]. A detailed formulation of the two-scale finite element simulation using the crystal plasticity constitutive equation is described in Supplementary Material and was based on a previously reported method [21].

2.2.2. Finite element model for numerical biaxial tensile test

The finite element model used for the numerical biaxial tensile tests is shown in Fig. 2. Two length-scales were defined, where the macroscopic scale was denoted by x_i ($i = 1, 2, 3$) and the microscopic scale by y_i ($i = 1, 2, 3$). The macroscale coordinate axes for $i = 1$, 2 and 3 were defined parallel to the RD, TD, and normal direction (ND) of the sheet, respectively. The finite element (FE) model for the macroscale (macro-FE model) consisted of a single hexagonal isoparametric element with eight integration points. The FE model for the microscale (micro-FE model) included a representative volume element for the crystallographic texture of a sheet and was described by a cubic domain. The micro-FE model was divided by 125 elements based on the same finite element type (isoparametric element with eight integration points) used for the macro-FE model. Thus, crystallographic texture consisting of 1000 crystal orientations was described in the micro-FE model. The initial 1000 crystal orientations were sampled from the EBSD measurement results (1,009,957 crystal orientations) based on the STAT method [57]. Fig. 3 shows the {111} pole figure of the 1000 crystal orientations used as the input data for the numerical biaxial tensile test (σ_{11}: $\sigma_{22} = 1{:}0$), which was performed to calibrate the strain-hardening parameters of the crystal plasticity constitutive equation. The same initial crystal orientation dataset was assigned to all integration points in the macro-FE model.

The material constants for 5182-O aluminum alloy and the parameters used in this study are listed in Table 1 [32]. A fixed strain sensitivity factor (m) of 0.005 was chosen because the strain sensitivity of aluminum alloy is generally low.

The strain-hardening parameters were calibrated using the numerical biaxial test (σ_{11}: $\sigma_{22} = 1{:}0$) and the nodal velocity along the RD was applied to the nodes of the macro-FE model to obtain a nominal strain rate (5.0×10^{-4} s^{-1}) similar to the experimental uniaxial tensile test. Further, the nodal forces in the numerical biaxial tensile tests were applied to the nodes of the macro-FE model along the RD and TD using the same algorithm as the experimental biaxial tensile test to ensure a constant true stress ratio. The plastic strain rate during biaxial tensile deformation was set in the order of 5.0×10^{-4} s^{-1}. The same seven linear stress paths evaluated in the experimental biaxial tensile tests were also evaluated using the numerical biaxial tensile tests (i.e. σ_{11}: σ_{22} = 4:1, 2:1, 4:3, 1:1, 3:4, 1:2 and 1:4). The macroscopic nominal stress was calculated by dividing the integrated value of the nodal forces on the surface of the macro-FE model with the initial cross-sectional area of the macro-FE model. The macroscopic nominal strain was calculated by dividing the change in the side length of the macro-FE model after deformation by the initial length.

2.2.3. Validation

As stated in the previous section, the strain-hardening parameters in Eq. (18) were identified by fitting the true stress-true strain curve obtained from the numerical biaxial tensile test (σ_{11}: $\sigma_{22} = 1{:}0$) to the experimental uniaxial stress-strain curve for the RD of the 5182-O aluminum alloy sheet. In Fig. 4 (a), the calculated stress-strain curve is compared with the experimental result. From the fitting of the curves, we identified the strain-hardening parameters which are listed in Table 2. Furthermore, the true stress-true strain curve for TD was calculated using numerical biaxial tensile test (σ_{11}: $\sigma_{22} = 0{:}1$) based on the identified parameters, and the results are compared with the experimentally obtained curve as shown in Fig. 4(b).

Biaxial true stress-logarithmic plastic strain curves were calculated using the calibrated numerical biaxial tensile tests. The calculated stress-strain curves displayed high correlation with the experimental results at true stress ratios of σ_{11}: σ_{22} = 4:1, 3:4, 1:2, and 1:4 (see Fig. 5). However, the numerical biaxial tensile tests slightly overestimated the true stress at the other stress ratios. Overall, the numerical biaxial tensile tests provided a reasonably accurate prediction of biaxial tensile testing. Therefore, numerical biaxial tensile tests with the parameters listed in Table 2 were used to generate the DNN training

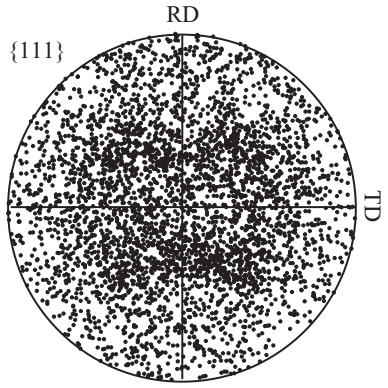

Fig. 3. {111} pole figure of the initial 1000 crystal orientations used as the input data in the numerical biaxial tensile test (σ_{11}: $\sigma_{22} = 1{:}0$), which was performed to calibrate the strain-hardening parameters of the crystal plasticity constitutive equation. The initial crystal orientations were sampled from the results of EBSD measurement.

Table 1
Material constants for 5182-O aluminum alloy and parameters used in this study.

Elastic constants [GPa] (Voigt notation)	$C_{11} = 108.2$ $C_{12} = 61.3$ $C_{44} = 28.5$
Reference shear rate, $\dot{\gamma}_0$ [s^{-1}]	0.5
Strain rate sensitivity factor, m	0.005

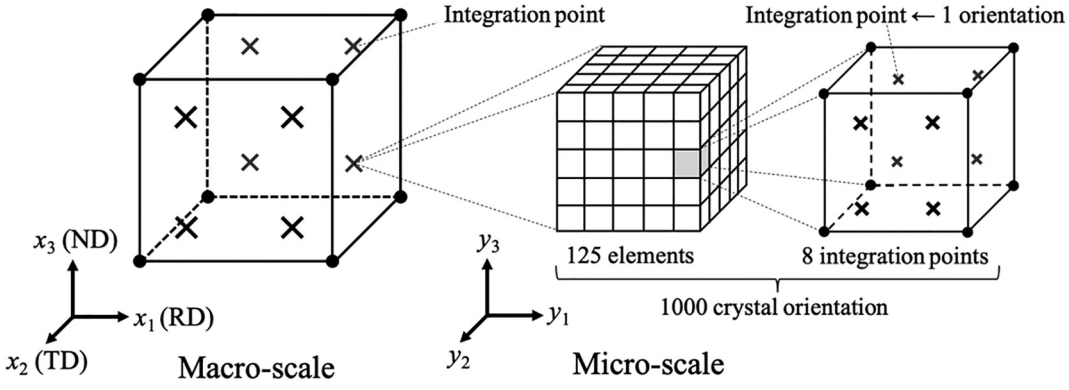

Fig. 2. The macro- and microscale finite element models for the numerical biaxial tensile tests.

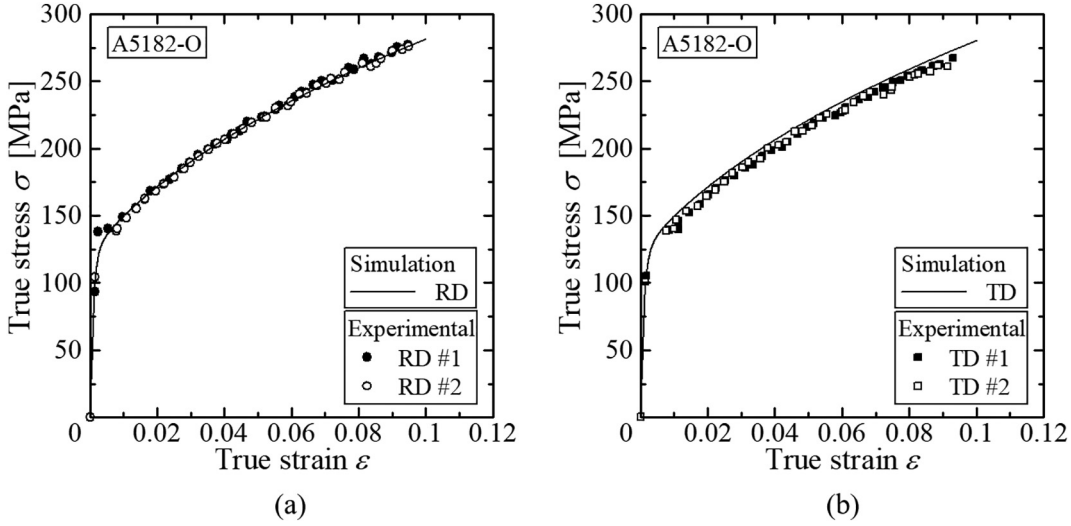

Fig. 4. True stress-true strain curves obtained from experiment (uniaxial tensile test) and numerical biaxial tensile test for the (a) RD and (b) TD of 5182-O aluminum alloy at a true stress ratio of σ_{11}:σ_{22} = 1:0.

Table 2
Strain-hardening parameters calibrated based on the numerical biaxial tensile test at a true stress ratio of σ_{11}: σ_{22} = 1:0.

Initial CRSS, τ_0 [MPa]	45
Latent-hardening matrix, $q^{(\alpha\beta)}$	1.0
Initial hardening coefficient, h_0 [MPa]	115
Hardening index, n'	0.24
Hardening constant, C	17
Initial plastic shear strain, γ_{int}	0.1

and validation datasets. The main goal of this study was to demonstrate that DNNs can estimate biaxial stress-strain curves based on crystallographic texture with same accuracy as the numerical biaxial tensile tests. Therefore, it was assumed that the strain-hardening behavior and the corresponding parameters (see Table 2) were not affected by changes in crystallographic texture.

2.2.4. Training, validation, and test datasets

The development of a DNN machine-learning algorithm requires training, validation, and test datasets. During training, the DNN identifies patterns in a training dataset that includes input and output data. Here, the input data was comprised of true stress ratios and digital images of the synthetic crystallographic texture, while the output data was the biaxial true stress-logarithmic plastic strain curves calculated using the numerical biaxial tensile test. The validation dataset was used to optimize the weights and biases of the DNN, after which the test dataset was used for testing the performance of the trained DNN.

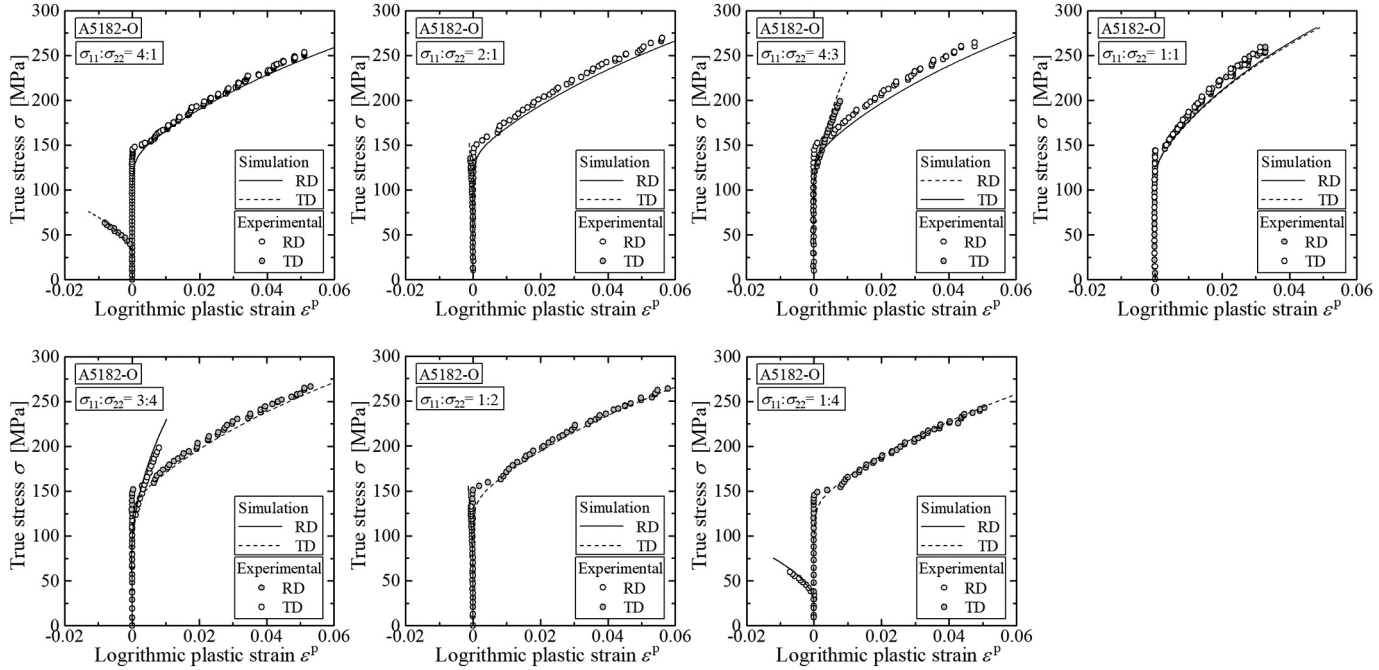

Fig. 5. Biaxial true stress-logarithmic plastic strain curves at seven true stress ratios calculated from experiments (biaxial tensile testing with a cruciform sample) and numerical biaxial tensile tests.

Table 3
Bunge Euler angle of the ideal orientations of the different preferred texture components.

Component	Euler angles (ϕ_1, ϕ, ϕ_2; °)
Cube {001}⟨100⟩	(0, 0, 0)
Goss {110}⟨001⟩	(0, 45, 0)
S {123}⟨634⟩	(59, 37, 63), (27, 58, 18), and (53, 75, 34)
Brass {110}⟨112⟩	(35, 45, 0) and (55, 90, 45)
Copper {112}⟨111⟩	(90, 35, 45) and (39, 66, 27)

It is important to note that the DNN was not further optimized during this independent testing step.

2.3. Crystallographic texture

2.3.1. Synthetic crystallographic texture

The synthetic crystallographic texture was based on five preferred texture components generally observed in aluminum alloys, namely Cube {001} ⟨100⟩, Goss {110}⟨001⟩, S {123}⟨634⟩, Brass {110} ⟨112⟩, and Copper {112} ⟨111⟩. Cube and Goss are recrystallization texture components, whereas S, Brass, and Copper are deformation texture components. The Bunge Euler angles (ϕ_1, ϕ, and ϕ_2) of the ideal orientations of each texture component are given in Table 3.

The synthetic texture was modeled using a three-dimensional Gaussian distribution function based on the ideal orientations given in Table 3. The Gaussian distribution function is expressed as:

$$f(\phi_1,\phi,\phi_2) = \frac{1}{\left(\sqrt{2\pi}\right)^3 \zeta_i^3} \exp\left(-\frac{\phi_1^2+\phi^2+\phi_2^2}{2\zeta_i^2}\right) \quad (19)$$

where ζ_i^2 (i = Cube, S, Goss, Brass, and Copper) denotes the variance of each preferred texture component in the synthetic texture with respect to the ideal orientation. The synthetic texture was determined using Eq. (19) as follows:

Step 1: The volume fraction (V_i) and variance (ζ_i^2) (i = Cube, S, Goss, Copper, and Brass) of each texture component in the synthetic texture were determined. The number of crystal orientations of each texture component ($N_{\mathrm{ori}}^{(i)}$) in the synthetic texture was calculated as $N_{\mathrm{ori}}^{(i)} = 1000V_i$.

Step 2: Three random real numbers (a, b, c) between 0 and 1 were generated from a Gaussian distribution with mean = 0 and variance = 1.

Step 3: The real numbers generated in Step 2 were multiplied by the standard deviation (ζ_i) to determine the random orientation (ϕ'_1, ϕ', ϕ'_2; °).

Step 4: The ideal orientation of the texture component was added to the random orientation obtained in Step 3 to give the synthetic texture orientation (ϕ_1, ϕ, ϕ_2) (e.g. orientation angle (ϕ_1, ϕ, ϕ_2) = (ϕ'_1 + 59°, ϕ' + 37°, ϕ'_2 + 63°) for the S-component).

Step 5: Steps 2 to 4 were repeated for all the crystal orientations.

Various synthetic textures were generated by changing the volume fraction of the preferred texture component in the synthetic texture (V_i) in 10% increments from 0% to 100%. If the sum of the volume fractions of the preferred texture components was less than 100%, the remainder was attributed to a random component. The variance (ζ_i^2) in Step 1 was changed every 5 deg^2 from 5 to 15 deg^2, as described in a previously reported method by Wu et al. [58]. A total of 5944 synthetic textures were generated for the training and validation datasets.

For the test dataset, synthetic texture was generated by changing the volume fraction of the preferred texture components (V_i) in 10% increments from 0% to 60%, while the variance (ζ_i^2) was changed every 5 deg^2 from 5 to 15 deg^2. A total of 252 synthetic textures were generated for the test dataset.

2.3.2. Pole figure of synthetic crystallographic texture

DNN-2D was developed to estimate biaxial stress-strain curves from a digital image of the {111} pole figure of a synthetic texture. The digital image of a {111} pole figure was generated as follows (see Fig. 6):

Step 1: The position of the pole (Q(x, y)) for a crystal orientation in the synthetic texture was determined via stereographic projection.

Step 2: The projection plane was divided into $N^2 = 2^n \times 2^n$ sub-domains, where the number of sub-domains corresponded to the resolution of the digital image of the {111} pole figure.

Step 3: The sub-domain, Q(i, j), containing the pole, Q(x, y), was determined, where i (i = 1–2^n) and j (j = 1–2^n) denote the indices of the sub-domain.

Step 4: Steps 1, 2, and 3 were repeated for all the crystal orientations in the synthetic texture.

Step 5: The number of poles in each sub-domain was calculated and denoted as $M(i,j)$. The luminance of each pixel in the digital image of the {111} pole figure was calculated as $L(i,j) = 255\,M(i,j)/a$. The value of a is fixed, where a value of 10 was used in this study.

A small proportion (0.01%) of the calculated pole figures contained pixels with a luminance value above 255. The luminance of these pixels was corrected to 255.

Fig. 7 shows the digital images of {111} pole figures produced by the above procedure, in which the synthetic texture consisted of a single preferred texture component. The gray scale represents the integration degree of the texture component. High resolution pole figure images can generate a large computational load during DNN training and estimation of biaxial stress-strain curves using the trained DNN. Therefore, the effect of pole figure image resolution on estimation accuracy was evaluated by trial-and-error. A preliminary investigation indicated that a {111} pole figure image resolution of 128 × 128 pixels (i.e. n = 7) was most suitable.

The digital images of the {111} pole figures were converted via monochrome inversion during the training of DNN-2D, which follow the Modified National Institute of Standards and Technology (MNIST)

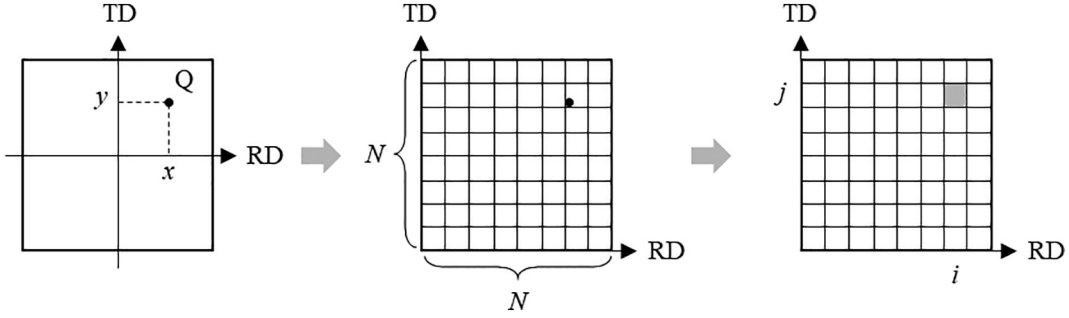

Fig. 6. Schematic diagram of the procedure for creating a digital image of a {111} pole figure.

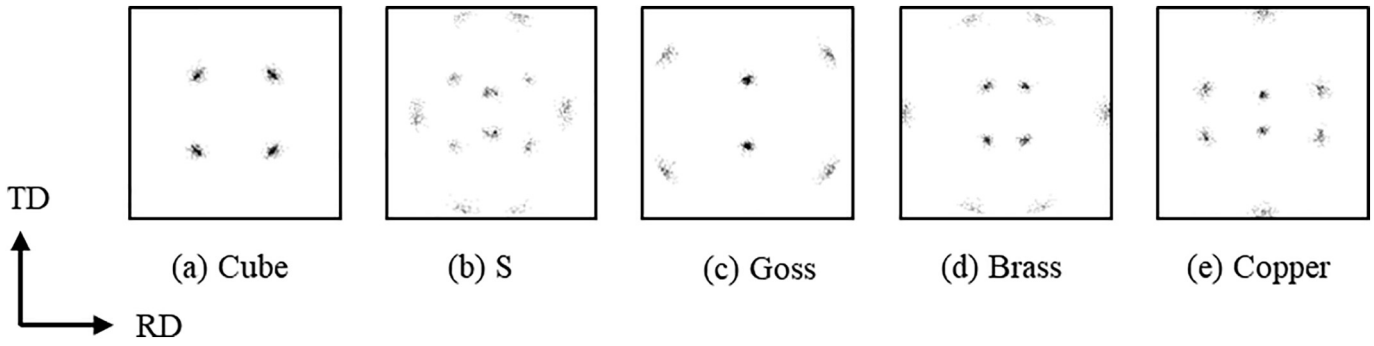

Fig. 7. Digital images generated from {111} pole figures in which the synthetic texture consisted of a single preferred texture component, namely (a) Cube, (b) S, (c) Goss, (d) Brass, and (e) Copper. The pole figures were generated at a constant volume fraction ($V_i = 100\%$) and variance ($\zeta_i^2 = 10\ \mathrm{deg}^2$), where i = Cube, S, Goss, Brass, and Copper.

dataset [59]. The 5944 pole figure digital images generated for all the synthetic textures were saved in portable network graphics (PNG) format.

2.3.3. 3D orientation map of synthetic crystallographic texture

The 3D images of the synthetic texture used as the input data for DNN-3D were created using the following procedure:

Step 1: The position of crystal orientations in the synthetic texture was calculated in a 3D Euler angle space ranging $0° \leqq \phi_1 \leqq 360°$, $0° \leqq \phi \leqq 180°$, and $0° \leqq \phi_2 \leqq 360°$ (see Fig. 8(a)).

Step 2: The 3D Euler angle space was divided into $N_x \times N_y \times N_z$ voxels.

Step 3: The orientation densities (ρ_i) of the ith ($i = 1, 2, \ldots, N_x \times N_y \times N_z$) voxel were calculated as $\rho_i = n_i / b$, where n_i is the number of orientations in the ith voxel and b is a constant for regularizing ρ_i between 0 and 1. A matrix of orientation density (ρ_i) was used to train DNN-3D.

The number of voxels in the 3D Euler angle space was $N_x \times N_y \times N_z = 32 \times 16 \times 32$, thus the total number of voxels was equal to the resolution of the digital image of {111} pole figure ($2^7 \times 2^7$). A b-value of 40 was used to ensure that the synthetic texture was only observed when the orientation density (ρ_i) was larger than 1, thus the orientation density was correct to 1. An example of a 3D image of a synthetic texture comprising a single Goss component with a variance of $\zeta^2_{\mathrm{Goss}} = 10\ \mathrm{deg}^2$ is shown in Fig. 8(b). The 3D image data of a synthetic texture is hereafter referred to as 3D orientation map.

2.3.4. Biaxial true stress-logarithmic plastic strain curves

The training and validation datasets contained biaxial true stress-logarithmic plastic strain curves calculated using the numerical biaxial tensile tests based on synthetic texture. A total of 53,496 stress-strain curves were generated by performing the numerical biaxial tensile tests at 9 true stress ratios, namely σ_{11}: σ_{22} = 1:0, 4:1, 2:1, 4:3, 1:1, 3:4, 1:2, 1:4, and 0:1, based on 5944 synthetic textures. The test data contained biaxial true stress-logarithmic plastic strain curves calculated using the numerical biaxial tensile tests based on 252 synthetic textures, thus producing a total of 2268 stress-strain curves (252 textures × 9 true stress ratios).

The dimensions of output data from the trained DNNs was reduced by processing the biaxial stress-strain curves as follows:

Step 1: Non-dimensional true stress-logarithmic plastic strain curves were calculated by normalizing the true stress-logarithmic plastic strain curves obtained from the numerical biaxial tensile tests by their maximum values ($\sigma_{\max}$ and $\varepsilon^p_{\max}$).

Step 2: The non-dimensional true stresses ($\overline{\sigma}_i$; $i = 1, 2, \ldots, n_{\mathrm{div}}$) at equal intervals between 0.5 and 1.0 and the corresponding non-dimensional logarithmic plastic strain ($\overline{\varepsilon}^p_0$; $i = 1, 2, \ldots, n_{\mathrm{div}}$) were calculated. Here, n_{div} is a constant.

Thus, the biaxial stress-strain curves were presented as a numerical sequence including $\overline{\sigma}_i$, $\overline{\varepsilon}^p_i$ ($i = 1, 2, \ldots, n_{\mathrm{div}}$), $\sigma_{\max}$ and $\varepsilon^p_{\max}$, where n_{div} was set to 50 in this study.

2.4. Deep learning method

2.4.1. Architecture of DNN-2D

DNN-2D was developed to estimate biaxial stress-strain curves from a digital image of the {111} pole figure representing synthetic texture (see Fig. 9). The six-layered DNN-2D was based on a similar DNN reported by Koenuma et al. [46], and consisted of convolution, max pooling, and fully connected layers. A convolution layer and a max

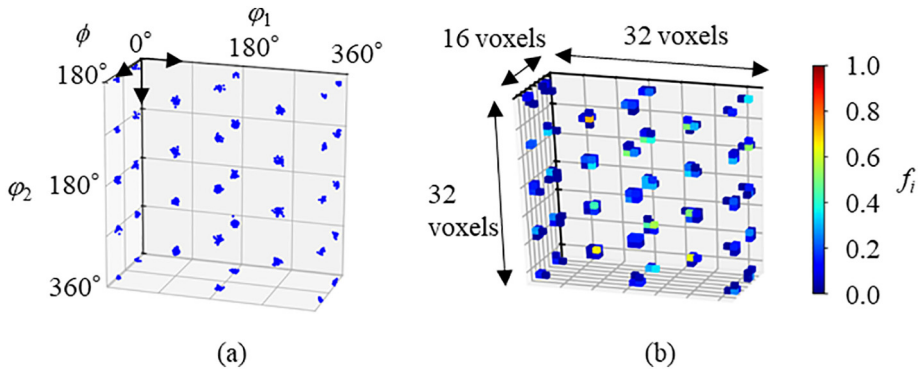

Fig. 8. (a) 3D plot of a synthetic texture containing a single Goss component ($\zeta^2_{\mathrm{Goss}} = 10\ \mathrm{deg}^2$) in the 3D Euler angle space. (b) The corresponding 3D orientation map of the synthetic texture with the distribution of orientation density (ρ_i) in the voxelized Euler angle space.

pooling layer were used in the first layer to receive the input image (128 × 128 pixels). A filter size of 7 × 7 and the stride value of 3 was used in the convolution layer, while a filter size of 3 × 3 was used in the max pooling layer. Thus, 16 images of 14 × 14 pixels were obtained to extract the features of the input {111} pole figure. The second layer converted these 16 images to 32 images of 6 × 6 pixels using a convolution layer with a filter size of 5 × 5 and a stride value of 2. The third layer compressed the 32 images into 64 images of 1 × 1 pixel using a convolution layer with a filter size of 5 × 5 and stride value of 1, and a max pooling layer with a filter size of 2 × 2. This layer further captured the features of the {111} pole figure image. The fourth layer combined the 64 images and corresponding true stress ratio (i.e. σ_{11}: σ_{22}) with a fully connected layer of 512 units. The nine true stress ratios (σ_{11}: σ_{22} = 1:0, 4:1, 2:1, 4:3, 1:1, 3:4, 1:2, 1:4, and 0:1) were converted to real numbers (0, 0.125, 0.25, 0.375, 0.5, 0.625, 0.75, 0.875, and 1, respectively). The neural network included two-branches to output the non-dimensional logarithmic plastic strains ($\bar{\varepsilon}_i^p$; i = 1, 2, …, n_{div}), maximum true stress ($\sigma_{\max}$) and logarithmic plastic strain ($\varepsilon_{\max}^p$) values in the output layer. The fifth layer was a fully connected layer with 512 units to improve the regression accuracy of the non-linear training data, whereas the sixth layer was a fully connected layer to output the normalized logarithmic plastic strain ($\bar{\varepsilon}_i^p$), maximum true stress ($\sigma_{\max}$), and maximum logarithmic plastic strain ($\varepsilon_{\max}^p$) for RD and TD.

In DNN-2D and DNN-3D, the convolution was followed by batch normalization [60,61] in the first, second and third layers. Further, the exponential linear unit (ELU) [62] was used as an activation function for all layers except for the output layer. The mean squared error (MSE) of the loss function was applied in DNN-2D and DNN-3D.

DNN-2D was constructed and trained in the Neural Network Console developed by Sony Network Communications Inc. [63]. The detailed specifications of the layers used in DNN-2D are given in the web reference [64] and the trained DNN-2D, the training parameters, and the datasets used for training and validation are freely available at https://github.com/Yamanaka-Lab-TUAT/DNN-NMT [47].

2.4.2. Architecture of DNN-3D

DNN-3D was developed to estimate biaxial stress-strain curves from the 3D orientation map of a synthetic texture (see Fig. 10). The DNN consisted of six layers and was constructed based on Keras [65] framework. The first layer consisted of a convolution layer and a max pooling layer to receive the input data (3D orientation map). The convolution layer had a filter size of 7 × 7 × 7 and a stride value of 1, while the max pooling layer had a filter size of 2 × 1 × 1. The input data was converted to 16 voxel datasets of 14 × 12 × 14. The second layer converted the 16 voxel datasets to 32 voxel datasets of 6 × 5 × 6 using a convolution layer with a filter size of 5 × 5 × 5 and a stride value of 2. The third layer further compressed the 16 voxel datasets to 64 voxel datasets of 1 × 1 × 1 using a convolution layer with a filter size of 5 × 5 × 5 and a stride value of 1, and a max pooling layer with a filter size of 2 × 1 × 2. The fourth, fifth and sixth layers applied were same as those employed in DNN-2D.

If a larger number of intermediate layers were to be included, the estimation accuracy of the biaxial stress-strain curves is expected to improve. However, it can result in overtraining due to increase in the number of optimized weights and bias. A preliminary investigation of the effect of the number of intermediate layers on the estimation accuracy was conducted by including 1, 2, and 3 intermediate layers. The estimation accuracy did not improve when 3 intermediate layers were used, thus 2 intermediate layers (i.e., fourth and fifth layers) were chosen. The number of units in the intermediate layers were evaluated in the range 256 to 1024, thus confirming that 512 units was suitable.

2.4.3. Training and validation of DNN-2D and DNN-3D

DNN-2D and DNN-3D were trained using a mini-batch-based training scheme based on the Adam optimization algorithm [66].

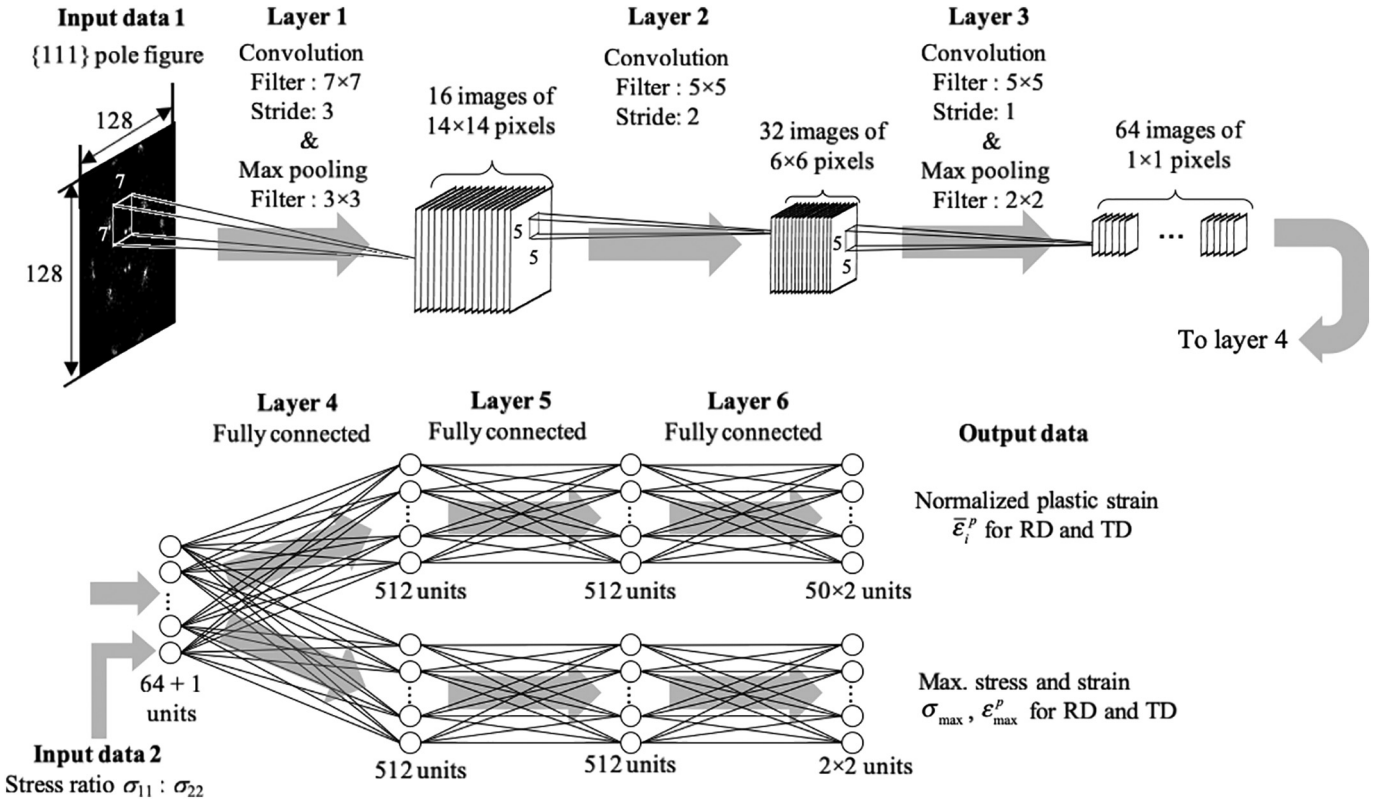

Fig. 9. Schematic illustration of DNN-2D for estimating biaxial stress-strain curves from a digital image of the {111} pole figure representing a synthetic texture.

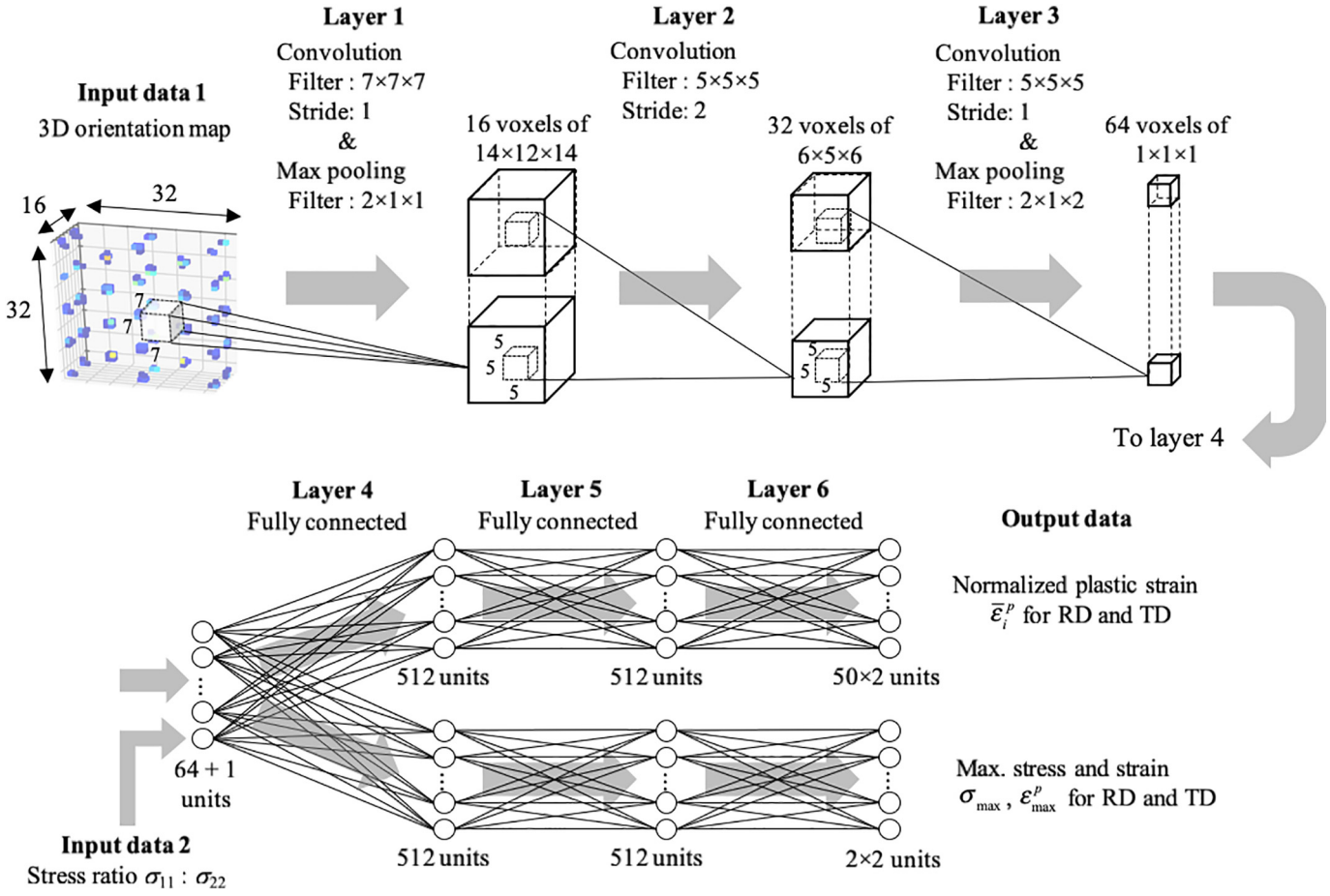

Fig. 10. Schematic illustration of DNN-3D for estimating biaxial stress-strain curves from a 3D orientation map of a synthetic texture.

A mini-batch size of 256 was chosen based on a preliminary evaluation of various mini-batch sizes (64, 128 and 256).

The resulting curves exhibited variations in the loss function (MSE) during the training and validation of the DNNs (Fig. 11). Training was terminated at 6000 epochs for DNN-2D and 3000 epochs for DNN-3D, where a full day was required for 5000 epochs using a graphic processing unit (NVIDIA TITAN V). The optimized weights and biases used for the estimation of the biaxial stress-strain curves were determined after 1060 epochs and 1330 epochs during the validation of DNN-2D and DNN-3D, respectively.

3. Results

3.1. Synthetic textures for testing the trained DNNs

Table 4 shows the volume fraction (V_i) and the variance (ζ_i^2) of the preferred texture components in three synthetic textures (Textures A, B, and C) used to test the trained DNNs. The three synthetic textures were not included in the training or validation datasets. The volume fraction and the variance of Textures A, B, and C were determined based on the texture of previously reported aluminum alloy sheets

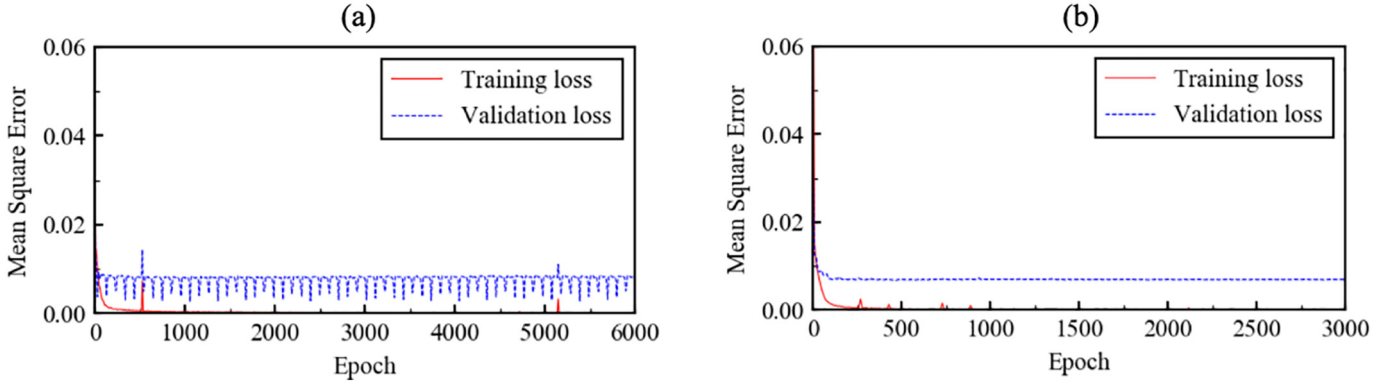

Fig. 11. Variation in the loss function (MSE) during the training and validation of (a) DNN-2D and (b) DNN-3D, where the red and blue lines represent the training and validation curves, respectively. (For interpretation of the references to colour in this figure legend, the reader is referred to the web version of this article.)

Table 4
Volume fraction (V_i) and the variance (ζ_i^2) of the preferred texture components in the synthetic textures (A, B, and C) used to test the trained DNN-2D and DNN-3D.

	Cube		S		Goss		Brass		Copper		Random
	V_{cube}	ζ^2_{cube}	V_S	ζ^2_S	V_{Goss}	ζ^2_{Goss}	V_{Brass}	ζ^2_{Brass}	V_{Copper}	ζ^2_{Copper}	V_{Random}
Texture A	6%	11 deg^2	29%	7 deg^2	5%	7 deg^2	15%	7 deg^2	15%	7 deg^2	30%
Texture B	5%	14 deg^2	41%	9 deg^2	4%	6 deg^2	22%	9 deg^2	16%	11 deg^2	12%
Texture C	18%	13 deg^2	8%	8 deg^2	10%	12 deg^2	2%	13 deg^2	4%	5 deg^2	58%

[67]. Examples of the digital images of the {111} pole figures and the 3D orientation maps for Textures A, B, and C are shown in Figs. 12 and 13, respectively. The major texture component in Textures A and B was the S-component, while Texture C contained a large volume fraction of the Cube-component and random texture.

The trained DNN-2D and DNN-3D were tested by comparing the estimated biaxial stress-strain curves with those calculated using the numerical biaxial tensile tests. The crystal orientations in the synthetic textures were dependent on the random numbers which were used to generate the synthetic textures. Thus, five sets of synthetic textures were generated based on the volume fraction and the variance listed in Table 4. The five generated synthetic textures were used as initial crystal orientations in the numerical biaxial tensile tests. The biaxial stress-strain curves obtained from the numerical biaxial tensile tests were used as the reference data for the trained DNN estimations.

The accuracy of the biaxial stress-strain curves estimated by the trained DNNs was evaluated based on 50 {111} pole figures and 3D orientation maps of Textures A, B, and C generated using the volume fractions and variances listed in Table 4. The pole figures and the 3D orientation maps were used as input data for the trained DNNs and biaxial stress-strain curves were estimated. The estimated mean biaxial stress-strain curve was compared with the numerical biaxial tensile test results.

3.2. Estimation of biaxial stress-strain curves using the trained DNNs

The biaxial true stress-logarithm plastic strain curves for Texture A estimated using the trained DNN-2D are given in Fig. 14. The trained DNN-2D provided an accurate estimation in comparison to the biaxial stress-strain curves calculated from the numerical biaxial tensile tests for all values of the stress ratios. Further, as shown in Fig. 15, the biaxial true stress-logarithm plastic strain curves were estimated by the trained DNN-3D with the same accuracy as the trained DNN-2D.

The results obtained from the trained DNN-2D and DNN-3D were quantitatively compared based on the contours of equal plastic work in the stress space. This approach was first introduced by Hill and Hutchinson [68] and has been widely applied to evaluate the work-hardening behavior of sheet metals subjected to biaxial loading. The comparison between the work contours calculated from the biaxial stress-strain curves estimated by the trained DNNs and the numerical biaxial tensile tests for Textures A, B, and C is illustrated in Fig. 16. Although the estimated work contours deviated slightly from the reference data at stress ratios of σ_{11}: σ_{22} = 4:1 and 1:2, the results of the DNNs were in good agreement with the numerical biaxial tensile test results.

The estimation capability of the trained DNNs was evaluated based on the root mean squared error (RMSE) calculated as follows:

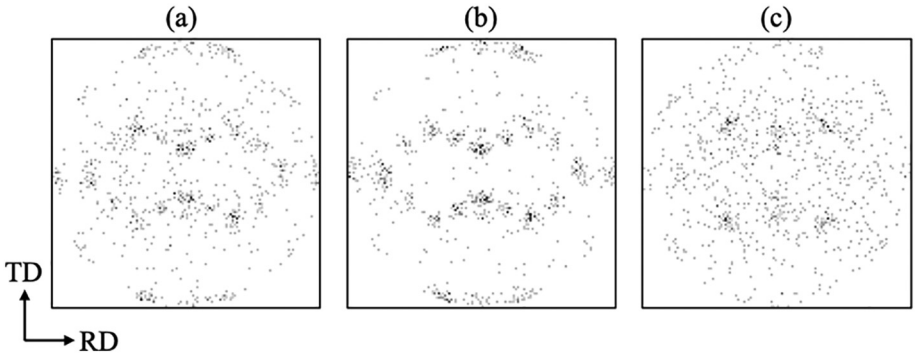

Fig. 12. Example of digital images of {111} pole figure for Textures (a) A, (b) B, and (c) C.

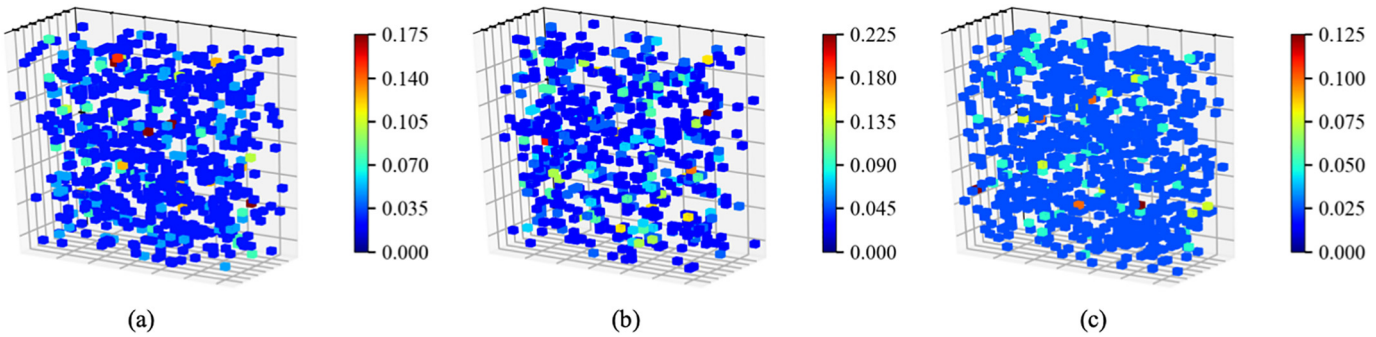

Fig. 13. Example of 3D orientation maps for Textures (a) A, (b) B, and (c) C.

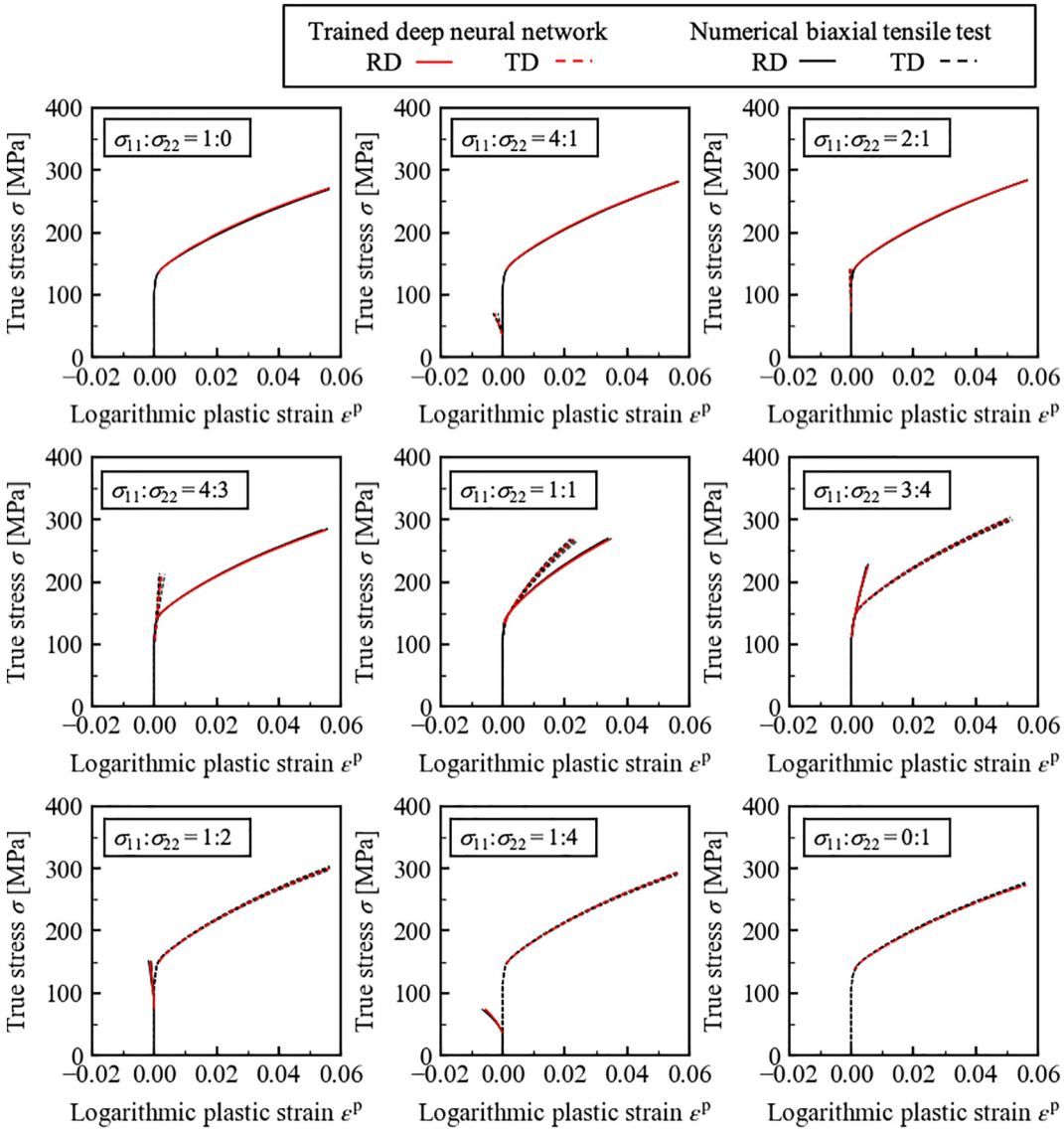

Fig. 14. Biaxial true stress-logarithmic plastic strain curves for Texture A calculated using the numerical biaxial tensile tests (black) and estimated by the trained DNN-2D (red). (For interpretation of the references to colour in this figure legend, the reader is referred to the web version of this article.)

$$\mathrm{RMSE}_j = \sqrt{\frac{1}{N_{\mathrm{test}}}\sum_{i=1}^{N_{\mathrm{test}}}(d_{ij})^2} \tag{20}$$

where j ($j = 1, 2, \ldots, 9$) is the index number of nine true stress ratios, viz. σ_{11}: σ_{22} = 1:0, 4:1, 2:1, 4:3, 1:1, 3:4, 1:2, 1:4, and 0:1. As shown in Fig. 17(a), d_{ij} is the difference between the stress points consisting the work contours calculated from the DNN and numerical biaxial tensile test results for the jth stress path; i (i = 1, 2, 3, …, N_{test}) denotes the ith test dataset and N_{test} is the number of the test datasets (i.e. $N_{\mathrm{test}} = 252$).

The RMSE for $\varepsilon_0^{\mathrm{p}} = 0.01$, 0.02, 0.03, and 0.04 is illustrated in Fig. 17 (b) and (c), which indicates that the RMSE increased with increase in $\varepsilon_0^{\mathrm{p}}$. Further, the RMSE for all stress ratios was less than 7 MPa, which corresponded to 3% of the maximum estimated true stress value. Furthermore, with the exception of σ_{11}: σ_{22} = 1:4 and σ_{11}: σ_{22} = 1:2, when $\varepsilon_0^{\mathrm{p}} = 0.01$, the RMSE of the work contours estimated by the trained DNN-3D were smaller than DNN-2D. These findings demonstrated that the trained DNN-3D provided a more accurate estimation than DNN-2D.

3.3. Computational efficiency of DNN-2D and DNN-3D

In the previous section, we showed that the trained DNN-3D can estimate the biaxial stress-strain curves and the work contour with a higher accuracy than DNN-2D for most of the stress ratios. This section compares the computational efficiency of DNN-2D and DNN-3D, which is an important aspect in the practical use of DNNs.

To compare the computational efficiency in the training of DNN-2D and DNN-3D, we measured the training time per epoch for DNN-2D using the profiling function of Neural Network Console [69]. On the other hand, the training time per epoch for DNN-3D was evaluated by averaging the training time required for 5 epochs, which was obtained by using Keras's callback function. The result elucidates that the training efficiency of DNN-2D (training time per epoch: 13.45 s) is better than that of the DNN-3D (training time per epoch: 23.43 s).

We further investigated the computational efficiency in the estimation of biaxial stress-strain curves using DNN-2D and DNN-3D by measuring the time spent for generating the curves for nine stress ratios using 50 sets of synthetic texture A. The result clearly shows that the estimation of biaxial stress-strain curves using DNN-2D

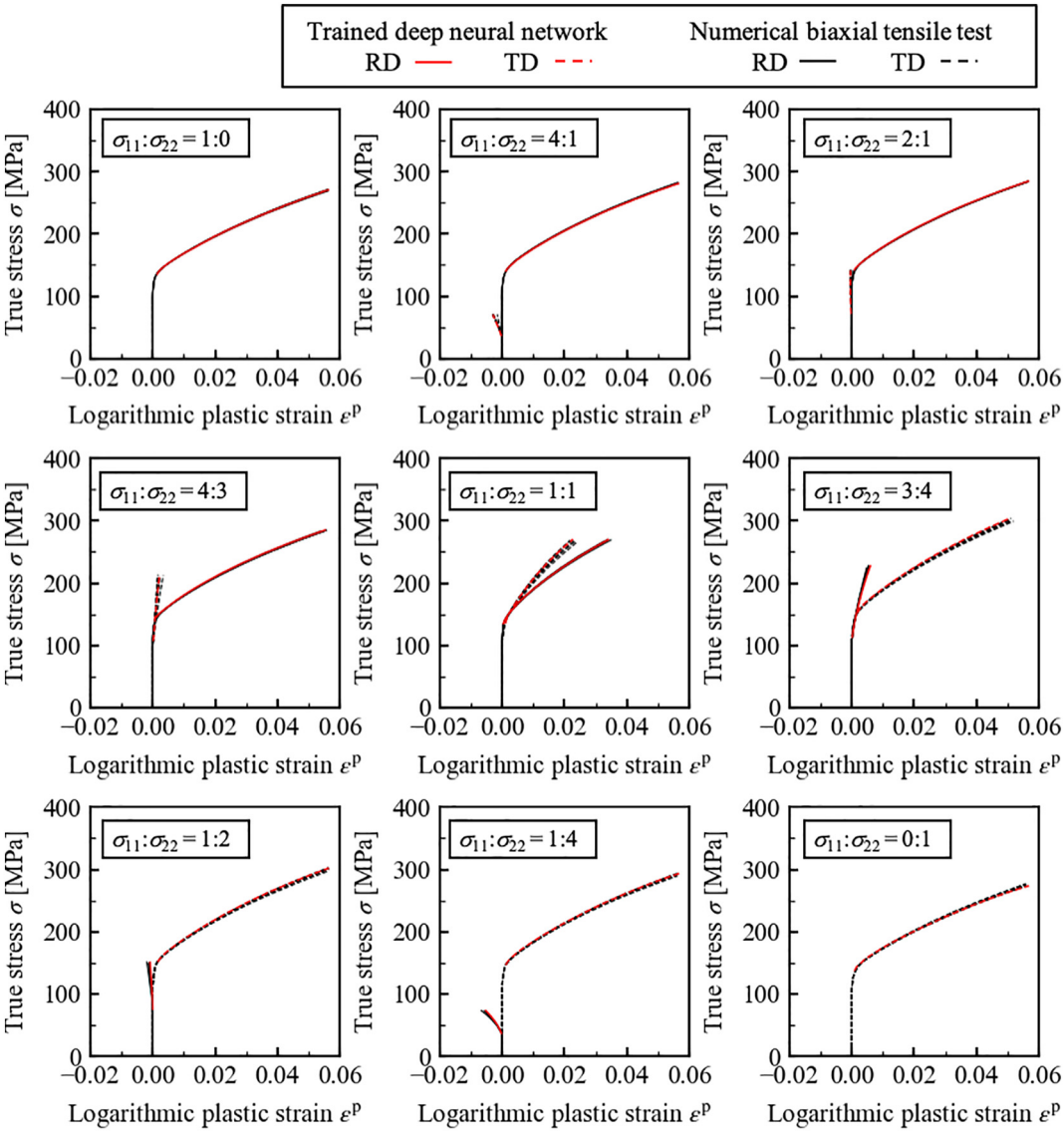

Fig. 15. Biaxial true stress-logarithmic plastic strain curves for Texture A calculated using the numerical biaxial tensile tests (black) and estimated by the trained DNN-3D (red). (For interpretation of the references to colour in this figure legend, the reader is referred to the web version of this article.)

(required time: 8.347 s) is faster than that of DNN-3D (required time: 12.560 s).

In summary, DNN-3D can estimate the biaxial stress-strain curve with a higher accuracy, though its computational efficiency is lower than that of DNN-2D. This decline in computational efficiency was expected since DNN-3D needs to perform the feature extraction of the 3D orientation map using the 3D convolution neural network.

4. Discussion

To calculate the biaxial stress-strain curves for nine true stress ratios, the numerical biaxial tensile tests requires at least one hour with parallel computing using multiple CPUs. On the other hand, the trained DNNs provided an accurate estimation of biaxial stress-strain curves for 50 synthetic textures in under a minute. The trained DNNs are computationally efficient tools for predicting biaxial tensile deformation behavior of aluminum alloy sheets without the use of any user-developed source codes for crystal plasticity simulations. Therefore, DNN is a promising method for generating virtual data in the material modeling of sheet metals.

The biaxial stress-strain curves estimated by the trained DNNs correlate well with the numerical biaxial tensile test results. However, as shown in Fig. 17(b) and (c), the RMSE at the stress ratio of σ_{11}: σ_{22} = 1:4 is higher than the RMSE at other stress ratios. To identify the origin of high RMSE, we examined the relationship between the synthetic textures in the test datasets and the RMSE. Table 5 shows the five synthetic textures for which we found the five highest values of d_{i8} (see Eq. (20)) at the reference plastic strain of $\varepsilon_0^p = 0.04$. It is clearly observed that the high d_{i8} correlates with a relatively high volume fraction of Goss-component ($V_{goss} \geq 50\%$). To further demonstrate the correlation between d_{i8} and V_{goss}, all biaxial stress-strain curves at the stress ratio of σ_{11}: σ_{22} = 1:4 in the training datasets are shown in Fig. 18; we also show the five biaxial stress-strain curves in the test datasets corresponding to the synthetic textures listed in Table 5. The five stress-strain curves for the TD (black solid lines in Fig. 18), which the trained DNNs could not accurately estimate, lies in the region with low training data density, resulting in high d_{i8} and consequently a high RMSE. Therefore, the high RMSE at the stress ratio of σ_{11}:σ_{22} = 1:4 shown in Fig. 17 can be reduced by increasing the training data density.

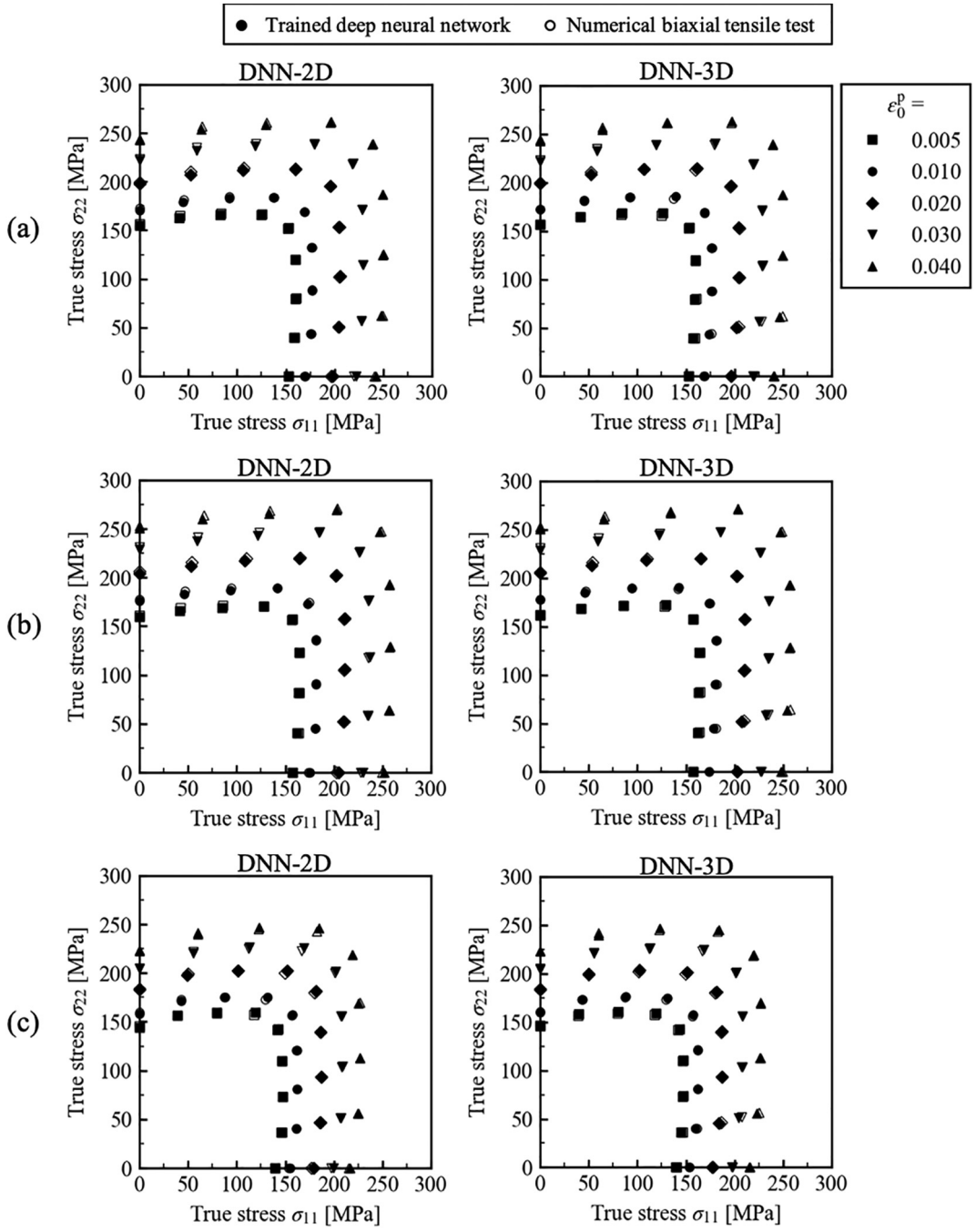

Fig. 16. Contours of equal plastic work calculated from the biaxial true stress-logarithmic plastic strain curves estimated by the trained DNNs and calculated using the numerical biaxial tensile tests for (a) Texture A, (b) Texture B, and (c) Texture C, where ε_0^p is the reference plastic strain and represents the logarithmic plastic strain in the uniaxial tensile state in RD (plastic work per unit volume).

The accuracy of the DNNs can be further improved. In this study, the {111} pole figure images were used as input data for DNN-2D, but the stereographic projection used to plot the pole figures may yield the same pole on a pole figure even if we use different crystal orientations. It was thus difficult for the DNN-2D to distinguish slight differences in the synthetic textures. The estimation accuracy of DNN-2D is expected to improve if multiple pole figures were used as for input images for DNN-2D, i.e. complementing the {111} pole figure with {100} and {110} pole figures.

It was assumed that changes in crystallographic texture did not affect the strain-hardening behavior of aluminum alloy sheets. On the contrary, the stress-strain curve of an aluminum alloy sheet is dependent on crystallographic texture, crystal grain size, precipitates, and other microstructures [70]. In particular, the dislocation density significantly affects stress-strain curve of aluminum alloy sheets. The estimation of biaxial stress-strain curves, which depends on such various microstructural factors, using a DNN approach requires sufficiently large database of microstructural data and stress-strain curves of various aluminum alloy sheets. Although some previous studies have developed databases for specific aluminum alloys [71,72], an appropriate database of the biaxial tensile deformation behavior of aluminum alloy sheets has not yet been developed. The development of a database containing experimental multiaxial stress test results is a major issue hindering the further development of the proposed DNN approach.

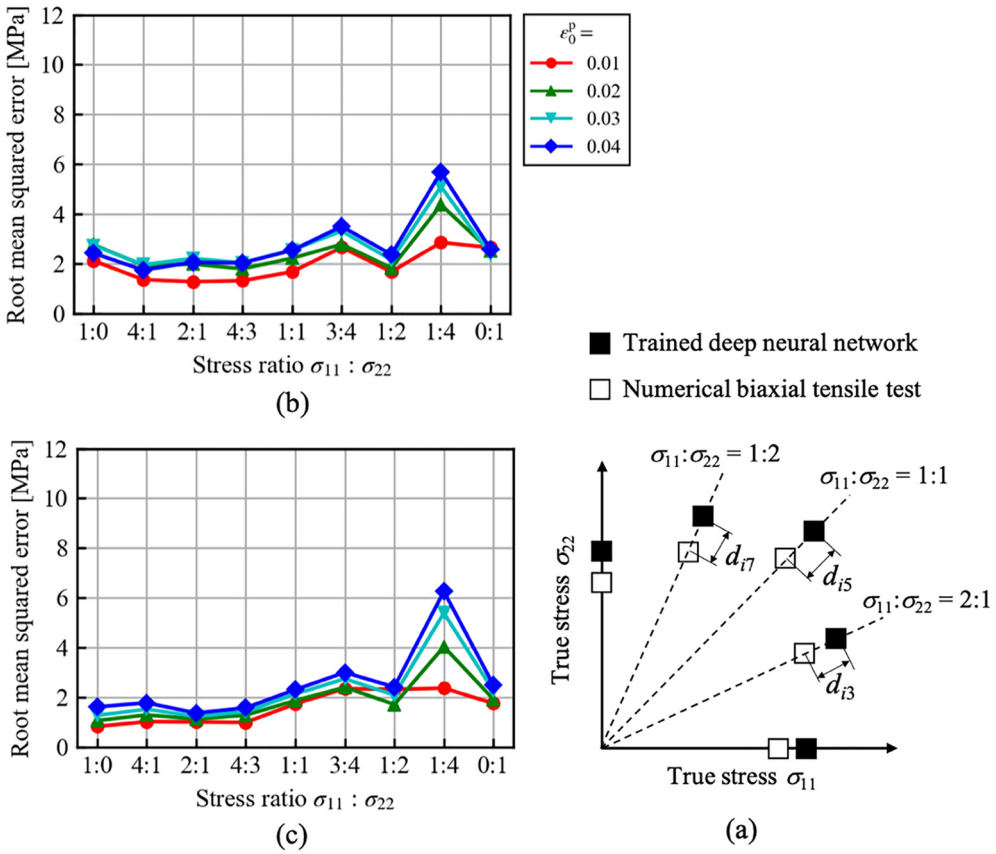

Fig. 17. (a) Schematic representation of d_{ij} used for calculating the RMSE (Eq. (20)). RMSE of the contours of equal plastic work estimated by the trained (b) DNN-2D and (c) DNN-3D with reference to the numerical biaxial tensile tests at different reference plastic strains (ε_0^p).

Table 5
Volume fraction (V_i) and variance (ζ_{Si}^2) of the five synthetic textures for which highest d_{i8} at the reference plastic strain of $\varepsilon_0^p = 0.04$ were observed in the test datasets. The texture ID corresponds to the index i of d_{i8}.

Texture ID	Cube		S		Goss		Brass		Copper		Random
	V_{cube}	ζ_{Scube}^2	V_S	ζ_{SS}^2	V_{Goss}	ζ_{SGoss}^2	V_{Brass}	ζ_{SBrass}^2	V_{Copper}	$\zeta_{SCopper}^2$	V_{Random}
51	10%	9 deg^2	10%	13 deg^2	60%	8 deg^2	10%	13 deg^2	10%	8 deg^2	0%
63	10%	10 deg^2	10%	10 deg^2	50%	6 deg^2	10%	13 deg^2	10%	14 deg^2	10%
134	20%	6 deg^2	10%	7 deg^2	50%	10 deg^2	10%	10 deg^2	10%	7 deg^2	0%
3	10%	5 deg^2	10%	11 deg^2	50%	12 deg^2	10%	14 deg^2	20%	13 deg^2	0%
90	10%	12 deg^2	10%	10 deg^2	50%	13 deg^2	10%	5 deg^2	10%	14 deg^2	10%

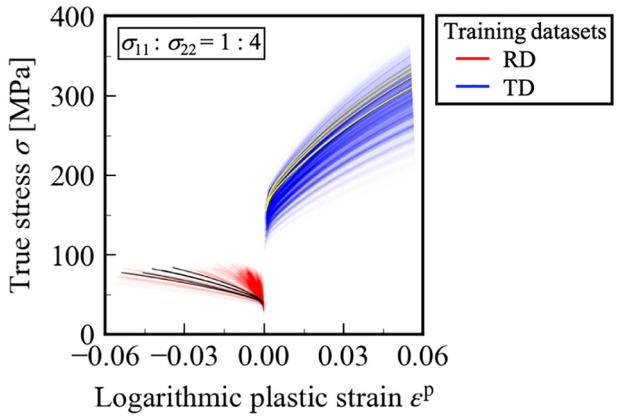

Fig. 18. Biaxial true stress-logarithmic plastic strain curves in the training datasets (red and blue lines); the opacity of the curves shows the training data density. Yellow and black solid lines show the biaxial stress-strain curves for RD and TD in the test datasets corresponding to the synthetic textures listed in Table 5. (For interpretation of the references to colour in this figure legend, the reader is referred to the web version of this article.)

Database development is a time-consuming task, but transfer learning [73–75] is a promising methodology for re-training a pre-trained DNN with a small experimental dataset. Nonetheless, it should be emphasized that the DNNs developed in this study will contribute to future work.

5. Conclusions

The validity of DNN approach for efficient material modeling of sheet metals was demonstrated by performing numerical experiments. Specifically, two DNNs (DNN-2D and DNN-3D) were developed to estimate the biaxial true stress-logarithmic plastic strain curves of aluminum alloy sheets from images of crystallographic texture based on preferential texture components. The input image data included {111} pole figure images for DNN-2D and 3D orientation maps for DNN-3D. Training, validation and testing datasets were generated using numerical biaxial tensile tests based on CPFEM. The numerical biaxial tensile test was experimentally validated based on uniaxial and biaxial tensile tests of 5182-O aluminum alloy sheet. The biaxial stress-strain curves estimated by the trained DNNs highly correlated with those calculated by the

numerical biaxial tensile tests. The precision of DNN-2D and DNN-3D was compared based on work contours, which indicated that the DNN-3D is more accurate than DNN-2D. However, the computational efficiency of DNN-2D was found to be higher than that of DNN-3D.

This study has demonstrated that the proposed DNNs and other machine-learning procedures offer a new approach for the generation of virtual data aimed at material modeling of sheet metals. The application of proposed DNN based approach to real sheet metals relies on the development of a multiaxial material test database and the future work aims to retrain the DNNs with an improved database.

Data availability

The data that supports the results of this study are available from the corresponding author upon reasonable request.

Declaration of Competing Interest

The authors declare that they have no known competing financial interests or personal relationships that could have appeared to influence the work reported in this paper.

Acknowledgement

The authors would like to thank Prof. Hiroshi Utsunomiya of Osaka University for the EBSD measurements of 5182-O aluminum alloy sheet. This research was financially supported by JSPS Grant-in-Aid for Scientific Research (KAKENHI) (B) Grant Number JP17H03425 and JP20H02476.

Appendix A. Supplementary data

Supplementary data to this article can be found online at https://doi.org/10.1016/j.matdes.2020.108970.

References

[1] E. Tekkaya, State-of-the-art of simulation of sheet metal forming, J. Mater. Proc. Technol. 103 (2000) 14–22.
[2] M.A. Ablat, A. Qattawi, Numerical simulation of sheet metal forming: a review, Int. J. Adv. Manuf. Technol. 89 (2017) 1235–1250.
[3] R. Hill, A theory of the yielding and plastic flow of anisotropic metals, Proc. Royal Soc. Lond. A 193 (1948) 281–297.
[4] F. Barlat, R.C. Becker, Y. Hayashida, Y. Maeda, M. Yanagawa, K. Chung, J.C. Brem, D.J. Lege, K. Matsui, S.J. Murtha, S. Hattori, Yielding description for solution strengthened aluminum alloys, Int. J. Plasticity 13 (1997) 385–401.
[5] F. Yoshida, T. Uemori, A model of large-strain cyclic plasticity describing the Bauschinger effect and workhardening stagnation, Int. J. Plasticity 18 (2002) 661–686.
[6] F. Barlat, J.C. Brem, J.W. Yoon, K. Chung, R.E. Dick, D.J. Lege, F. Pourboghrat, S.H. Choi, E. Chu, Plane stress yield function for aluminum alloy sheets – part 1: theory, Int. J. Plasticity 19 (2003) 1297–1319.
[7] D. Banabic, H. Aretz, D.S. Comsa, L. Paraianu, An improved analytical description of orthotropy in metallic sheets, Int. J. Plasticity 21 (2005) 493–512.
[8] H. Vegter, A.H. Van den Boogaad, A plane stress yield function for anisotropic sheet material by interpolation of biaxial stress states, Int. J. Plasticity 22 (2006) 557–580.
[9] T. Kuwabara, Advances in experiments on metal sheets and tubes in support of constitutive modeling and forming simulations, Int. J. Plasticity 23 (2007) 385–419.
[10] International Organization for Standardization, Metallic Materials—Sheet and Strip—Determination of Biaxial Stress-strain Curve by Means of Bulge Test With Optical Measuring Systems (ISO Standard No. 16808:2014), https://www.iso.org/standard/57777.html 2014 (accessed on 24 June 2020).
[11] L.M. Alves, C.V. Nielsen, P.A.F. Martins, Revisiting the fundamentals and capabilities of the stack compression test, Exp. Mech. 51 (2011) 1565–1572.
[12] A. Makinde, L. Thibodeau, K.W. Neale, Development of an apparatus for biaxial testing using cruciform specimens, Exp. Mech. 32 (1992) 138–144.
[13] T. Kuwabara, S. Ikeda, K. Kuroda, Measurement and analysis of differential work hardening in cold-rolled steel sheet under biaxial tension, J. Mater. Proc. Tech. 80–81 (1998) 517–523.
[14] International Organization for Standardization, Metallic Materials – Sheet and Strip – Biaxial Tensile Testing Method Using a Cruciform Test Piece (ISO Standard No. 16842:2014), https://www.iso.org/standard/57812.html 2014 (accessed on 24 June 2020).
[15] T. Kubabara, F. Sugawara, Multiaxial tube expansion test method for measurement of sheet metal deformation behavior under biaxial tension for a large strain range, Int. J. Plasticity 45 (2013) 103–118.
[16] T. Kuwabara, A. Van Vael, E. Iizuka, Measurement and analysis yield locus and work hardening characteristics of steel sheets with different r-values, Acta Mater. 50 (2002) 3717–3729.
[17] T. Kuwabara, M. Kuroda, V. Tvergaard, K. Nomura, Measurement of subsequent yield surface of prestrained sheet metal, Acta Mater. 48 (2000) 2071–2079.
[18] D. Yanaga, T. Kuwabara, N. Uema, M. Asano, Material modeling of 6000 series aluminum alloy sheets with different density cube textures and effect on the accuracy of finite element simulation, Int. J. Solids Struct. 49 (2012) 3488–3495.
[19] F. Roters, P. Eisenlohr, L. Hantcherli, D.D. Tjahjant, T.R. Bieler, D. Raabe, Overview of constitutive laws, kinematics, homogenization and multiscale methods in crystal plasticity-element modeling: theory, experiments, applications, Int. J. Plasticity 58 (2010) 1152–1211.
[20] F. Roters, P. Eisenlohr, T.R. Bieler, D. Raabe, Crystal Plasticity Finite Element Methods in Materials Science and Engineering, Wiley-VCH Verlag Gmbh & Co., Weinheim, 2010.
[21] E. Nakamachi, N.N. Tam, H. Morimoto, Multi-scale finite element analyses of sheet metals by using SEM-EBSD measured crystallographic RVE models, Int. J. Plasticity 23 (2007) 450–489.
[22] T.J. Barrett, M. Knezevic, Deep drawing simulations using the finite element method embedding a multi-level crystal plasticity constitutive law: experimental verification and sensitivity analysis, Comput. Methods Appl. Mech. Eng. 354 (2019) 245–270.
[23] N. Guo, J. Wang, C.Y. Sun, Y.F. Zhang, M.W. Fu, Analysis of size dependent earing evolution in micro deep drawing of TWIP steel by using crystal plasticity modeling, Int. J. Mech. Sci. 165 (2020) 105200.
[24] Y. Shi, H. Jin, P.D. Wu, Analysis of cup earing for AA3104-H19 aluminum alloy sheet, Eur. J. Mech. A Solids 69 (2018) 1–11.
[25] D. Raabe, Y. Wang, F. Roters, Crystal plasticity simulation study on the influence of texture on earing in steel, Comput. Mater. Sci. 34 (2005) 221–234.
[26] I. Tikhovskiy, D. Raabe, F. Roters, Simulation of earing during deep drawing of an Al-3% Mg alloy (AA 5754) using a texture component crystal plasticity FEM, J. Mater. Proc. Tech. 183 (2007) 169–175.
[27] M. Kraska, M. Doig, D. Tikhomirov, D. Raabe, F. Roters, Virtual material testing for stamping simulations based on polycrystal plasticity, Comput. Mater. Sci. 46 (2009) 383–392.
[28] J. Gawad, D. Banabic, A. Van Bael, D. Comsa, M. Gologanu, P. Eyckens, P. Van Houtte, D. Roose, An evolving plane stress yield criterion based on crystal plasticity virtual experiments, Int. J. Plasticity 75 (2015) 141–169.
[29] F. Roters, M. Diehl, P. Shanthraj, P. Eisenlohr, C. Reuber, S.L. Wong, T. Maiti, A. Ebrahimi, T. Hochrainer, H.-O. Fabritius, S. Nikolov, M. Friák, N. Fujita, N. Grilli, K.G.F. Janssens, N. Jia, P.J.J. Kok, D. Ma, F. Meier, E. Werner, M. Sticker, D. Weygand, D. Raabe, DAMASK-the Dusseldorf Advanced Material Simulation Kit for modeling multi-physics crystal plasticity, thermal, and damage phenomena from the single crystal up to the component scale, Comput. Mater. Sci. 158 (2019) 420–478.
[30] F. Han, M. Diehl, F. Roters, D. Raabe, Using spectral-based representative volume element crystal plasticity simulations to predict yield surface evolution during large scale forming simulations, J. Mater. Proc. Technol. 277 (2020) 116449.
[31] B.H. Frodal, L.E.B. Dælhi, T. Børvik, O.S. Hopperstad, Modelling and simulation of ductile failure in textured aluminum alloys subjected to compression-tension load, Int. J. Plasticity 118 (2019) 36–69.
[32] K. Hashimoto, A. Yamanaka, J. Kawaguchi, T. Sakurai, T. Kuwabara, Biaxial tensile deformation simulation of 5000 series aluminum alloy sheet using crystal plasticity finite element method based on homogenization method and its experimental validation, J. Jpn. Inst. Light Met. 65 (2015) 196–203 (in Japanese).
[33] A. Yamanaka, K. Hashimoto, J. Kawaguchi, T. Sakurai, T. Kuwabara, Material modelling and forming simulation of 5182 aluminum alloy sheets using numerical biaxial tensile test based on homogenized crystal plasticity finite element method, J. Jpn. Inst. Light Met. 65 (2015) 561–567 (in Japanese).
[34] W. Liu, B.K. Chen, Y. Pang, A. Najafzadeh, A 3D phenomenological yield function with both in and out-of-plane mechanical anisotropy using full-field crystal plasticity spectral method for modelling sheet metal forming of strong textured aluminum alloy, Int. J. Solid Struct. 193-194 (2020) 117–133.
[35] K. Zhang, B. Holmedal, T. Manik, A. Saai, Assessment of advanced Taylor models, the Taylor factor and yield-surface exponent for FCC metals, Int. J. Plasticity 114 (2019) 144–160.
[36] S. Coppieters, T. Hakoyama, P. Eychens, H. Nakano, A. van Bael, D. Debruyne, T. Kuwabara, On the synergy between physical virtual sheet metal testing: calibration of anisotropic yield functions using a microstructure-based plasticity model, Int. J. Mater. Form. 12 (2019) 741–759.
[37] S. Yoshitake, V. Narayan, H. Harada, H.K.D.H. Bhadeshia, D.J.C. Mackay, Estimation of the γ and γ' lattice parameters in nickel-based superalloys using neural network analysis, ISIJ Int. 38 (1998) 495–502.
[38] H. Fujii, D.J.C. Mackay, H.K.D.H. Bhadeshia, Bayesian neural network analysis of fatigue crack growth rate in nickel base superalloys, ISIJ Int. 36 (1996) 1373–1382.
[39] H.K.D.H. Bhadeshia, Neural networks in materials science, ISIJ Int. 39 (1999) 966–979.
[40] N. Haghdadi, A. Zarei-Hanzaki, A.R. Khalesian, H.R. Abedi, Artificial neural network modeling to predict the hot deformation behavior of an A356 aluminum alloy, Mater. Design 49 (2013) 286–391.
[41] G. Allegri, Modelling fatigue delamination growth in fiber-reinforced composites: power-law equations or artificial neural networks? Mater. Design 155 (2018) 59–70.

[42] G. Liu, L. Wang, Y. Yi, L. Sun, L. Shi, S. Ma, Inverse identification of graphite damage properties under complex stress states, Mater. Design 183 (2019) 108135.
[43] C. Yang, Y. Kim, S. Ryu, G.X. Gu, Prediction of composite microstructure stress-strain curves using convolution neural network, Mater. Design. 189 (2020) 108509.
[44] A. Jenab, I.S. Sarraf, D.E. Green, T. Rahmaan, M.J. Worswick, The use of genetic algorithm and neural network to predict rate-dependent tensile flow behaviour of AA5182-O sheets, Mater. Design. 94 (2016) 262–273.
[45] U. Ali, W. Muhammad, A. Brahme, O. Skiba, K. Inal, Application of artificial neural network in micromechanics for polycrystalline metals, Int. J. Plasticity 120 (2019) 205–219.
[46] K. Koenuma, A. Yamanaka, I. Watanabe, T. Kuwabara, Estimation of texture-dependent stress-strain curve and *r*-value of aluminum alloy sheet using deep learning, Mater. Trans. (2020) (in print).
[47] Yamanaka Laboratory, Tokyo University of Agriculture and Technology, Deep Neural Network-based Numerical Material Test Project, https://github.com/Yamanaka-Lab-TUAT/DNN-NMT 2020. (Accessed 24 June 2020).
[48] D. Peirce, R.J. Asaro, A. Needleman, An analysis of nonuniform and localized deformation in ductile single crystals, Acta Metall. 30 (1983) 1087–1119.
[49] J. Pan, J.R. Rice, Rate sensitivity of plastic flow and implications for yield-surface vertices, Int. J. Solid Struct. 19 (1983) 973–987.
[50] U.F. Kocks, H. Mecking, The physics and phenomenology of strain hardening, Prog. Mater. Sci. 48 (2003) 171–273.
[51] D. Pierce, C.F. Shih, A. Needleman, A tangent modulus method for rate dependent solids, Comp. Structs. 18 (1984) 875–887.
[52] J.M. Guedes, N. Kikuchi, Preprocessing and postprocessing for materials based on the homogenization method with adaptive finite element methods, Comput. Methods Appl. Mech. Eng. 83 (1990) 143–198.
[53] K. Terada, N. Kikuchi, A class of general algorithms for multi-scale analysis of heterogeneous media, Comput. Methods Appl. Mech. Eng. 190 (2001) 5427–5464.
[54] K. Terada, K. Matsui, M. Akiyama, T. Kuboki, Numerical re-examination of the micro-scale mechanism of the Bauschinger effect in carbon steels, Comput. Mater. Sci. 31 (2004) 67–83.
[55] I. Watanabe, K. Terada, M. Akiyama, Two-scale analysis for deformation-induced anisotropy of polycrystalline metals, Comput. Mater. Sci. 32 (2005) 240–250.
[56] I. Watanabe, K. Terada, E.A. de Souza Neto, D. Peric, Characterization of macroscopic tensile strength of polycrystalline metals with two-scale finite element analysis, J. Mech. Phys. Solid. 56 (2008) 1105–1125.
[57] L.S. Tóth, P. van Houtte, Discretization techniques for orientation distribution functions, Textur. Microstruct. 19 (1992) 229–244.
[58] P.D. Wu, S.R. MacEwan, D.J. Lloyd, K.W. Neale, Effect of cube texture on sheet metal formability, Mater. Sci. Eng. A364 (2004) 182–187.
[59] Y. LeCun, L. Bottou, Y. Bengio, P. Haffner, Gradient-based learning applied to document recognition, Proc. IEEE 86 (1998) 2278–2324.
[60] I. Goodfellow, Y. Bengio, A. Courville, Deep Learning, MIT Press, Cambridge, MA, 2016.
[61] S. Ioffe, C. Szegedy, Batch normalization: accelerating deep network training by reducing internal covariate shift, Proc. ICML 32 (2015) 448–456.
[62] D.A. Clevert, T. Unterthiner, S. Hochreiter, Fast and accurate deep network learning by exponential linear units (ELUs), in: Y. Bengio, Y. LeCun (Eds.),4th International Conference on Learning Representations, ICLR2016, San Juan, Puerto Rico, May 2-4, 2016, Conference Track Proceedings 2016, pp. 1–14https://arxiv.org/abs/1511.07289.
[63] Sony, Neural Network Console, https://dl.sony.com/ 2020 (accessed on 24 June 2020).
[64] Sony, Neural Network Console: Layer Reference, https://support.dl.sony.com/docs/layer_reference/ 2020 (accessed on 24 June 2020).
[65] Keras, Python Deep Learning Library, https://keras.io/ 2020 (accessed on 24 June 2020).
[66] P.D. Kingma, J. Ba, Adam: a method for stochastic optimization, in: Y. Bengio, Y. LeCun (Eds.),3rd International Conference on Learning Representations, ICLR2015, San Diego, CA, USA, May 7-9, 2015, Conference Track Proceedings 2015, pp. 1–15-http://arxiv.org/abs/1412.6980.
[67] X.H. Zeng, M. Ahmad, O. Engler, Texture gradient, average texture, and plastic anisotropy in various Al–Li sheet alloys, Mater. Sci. Technol. 10 (1944) 581–591.
[68] R. Hill, J.W. Hutchinson, Differential hardening in sheet metal under biaxial loading: a theoretical framework, J. Appl. Mech. 59 (1992) S1–S9.
[69] Sony, Neural Network Console: Profiling Function, https://support.dl.sony.com/docs/tutorial-profiling-the-training-processing-time/ 2020 (accessed on 24 June 2020).
[70] T. Kuwabara, T. Mori, M. Asano, T. Hakoyama, F. Barlat, Material modeling of 6016-O and 6016-T4 aluminum alloy sheets and application to hole expansion forming simulation, Int. J. Plasticity 93 (2017) 164–186.
[71] M. Dixit, R.S. Mishra, K.K. Sankaran, Structure-property correlations in Al 7050 and Al 7055 high-strength aluminum alloys, Mater. Sci. Eng. A478 (2008) 163–172.
[72] J.K. Paik, K.J. Kim, J.H. Lee, B.G. Jung, S.J. Kim, Test database of the mechanical properties of mild, high- tensile and stainless steel and aluminium alloy associated with cold temperatures and strain rates, Ships Offshore Struct. 12 (2017) 5230–5256.
[73] X. Li, Y. Zhang, H. Zhao, C. Burkhart, L.C. Brinson, W. Chen, A transfer learning approach for microstructure reconstruction and structure-property predictions, Sci. Rep. 8 (2018) 13461.
[74] S. Wu, Y. Kondo, M. Kakimoto, B. Yang, H. Yamada, I. Kawajima, G. Lambard, K. Hongo, Y. Xu, J. Shiomi, C. Schick, J. Morikawa, R. Yoshida, Machine-learning-assisted discovery of polymers with high thermal conductivity using a molecular design algorithm, npj Comput. Mater. 5 (2019) 66.
[75] H. Yamada, C. Liu, S. Wu, Y. Koyama, S. Ju, J. Shimoi, J. Morikawa, R. Yoshida, Predicting material properties with little data using shotgun transfer learning, ACS Cent. Sci. 5 (2019) 1717–1730.